Veth, Peter, Ward, Ingrid, Manne, Tiina, Ulm, Sean, Ditchfield, Kane, Dortch, Joe, Hook, Fiona, Petchey, Fiona, Hogg, Alan, Questiaux, Daniele, Demuro, Martina, Arnold, Lee, Spooner, Nigel, Levchenko, Vladimir, Skippington, Jane, Byrne, Chae, Basgall, Mark, Zeanah, David, Belton, David, Helmholz, Petra, Bajkan, Szilvia, Bailey, Richard, Placzek, Christa, and Kendrick, Peter (2017) ***Early human occupation of a maritime desert, Barrow Island, north-west Australia.*** **Quaternary Science Reviews, 168 pp. 19-29.**

Appendix A. Supplementary data

Contents

A1.1 Radiocarbon dating

Accelerator mass spectrometry (AMS) radiocarbon age determinations on charcoal and shell were undertaken at the University of Waikato Radiocarbon Dating Laboratory and Australian Nuclear Science and Technology Organisation (ANSTO) (Table 1).

A1.1.1 Sample preparation and analysis

Waikato samples were pre-treated following standard AMS protocols (UCI KCCAMS, 2011a, b). Following pre-treatment, charcoal (~2 mm fragments) samples were converted to CO_2 in sealed quartz tubes by oxidation at 800°C, using pre-baked CuO in the presence of silver wire to absorb any SO_x and NO_x produced. Shell (< 3 mm fragments, 35–45 mg) were etched in 0.1M HCl at 80°C to remove ~45% of the surface. Cleaned shells were then tested for recrystallization by Feigl staining (Friedman, 1959) to ensure either aragonite, or a natural aragonite/calcite distribution was present in the shell (e.g. *Nerita* sp.). CO_2 was collected from shells by reaction with 85% H_3PO_4. Cryogenically separated CO_2 was then reduced to graphite with H_2 at 550°C using an iron catalyst. $\delta^{13}C$ was measured either on a LGR Isotope analyser CCIA-46EP or a Thermos Scientific MAT252 IRMS. Pressed graphite was analysed at the Keck Radiocarbon Dating Laboratory, University of California on a NEC 0.5MV 1.5SDH-2 AMS system (Southon et al., 2004).

At ANSTO, after visual inspection for the presence of any powdery, potentially extraneous, calcite deposition shell surfaces were physically cleaned by abrasion of 10–25% of thickness with a Dremel® tool followed by chemical etching of another 10% with 0.5M HCl for 1–5 minutes under sonication at room temperature (Hua et al., 2001). Feigl staining test (Friedman, 1959) was also done on cleaned aragonite shells similar to Waikato

procedure. Hydrolysis was performed with concentrated H_3PO_4 acid. First ~25% of evolving CO_2 was discarded to eliminate any surface diagenesis contamination and the remaining evolving CO_2 was cryogenically cleaned and collected for dating. Charcoal samples were subject to aggressive pre-treatment using the ABOX protocol (Bird et al., 2014). Twenty to 40 mg of charcoal was combusted in sealed quartz tubes at 900°C with the prebaked CuO and silver wire (Hua et al., 2001). The evolved CO_2 was also cryo-cleaned and then converted to graphite (Hua et al., 2004), and measured for ^{14}C on STAR AMS at ANSTO (Fink et al. 2004). Results were corrected for laboratory blanks (processed in the same way) and $\delta^{13}C$ isotopic fractionation, which was determined on residual material in the graphite targets after AMS analysis. The graphite targets relate solely to the graphite derived from the studied fractions. Stable isotope measurements were performed on a separate elemental analyser Elementar varioMICRO CUBE coupled to a Micromass Isoprime IRMS.

A1.1.2 Marine reservoir effects

A 8–10 mm-long and ~4 mm-wide sample was taken parallel to the margin of each shell using a Dremel® 3000 Rotary Tool fitted with a diamond wheel. This sample size is designed to avoid seasonal variation and give an average value (Culleton et al., 2006; Hogg et al., 1998; Petchey et al. 2008)

To calculate ΔR, the collection year of each shell sample (i.e. year of death) was converted to an equivalent global marine modelled age using the Marine13 calibration dataset (Reimer et al., 2013). ΔR values were calculated by deducting the equivalent global marine model age at the time of death of the shell sample from the conventional radiocarbon age

obtained (Stuiver et al., 1986). $\Delta R\sigma$ is the one-sigma estimate of uncertainty in the conventional radiocarbon age of the shell sample. See Ulm (2002) and Ulm et al. (2009) for further details.

The habitat and diet of the shellfish sampled for dating can have a major impact on the accuracy of radiocarbon ages. Deposit feeders, carnivores and algal grazers can all ingest carbon from a variety of sources which can become incorporated into shell structures through metabolic processes, potentially making the ^{14}C activity of these shells out of equilibrium with the ambient environment (Tanaka et al. 1986). This is of particular concern for the Boodie Cave shell samples as Barrow Island is comprised of ancient limestones containing very old carbon. Three limestone geological formations are extant on Barrow Island: Trealla Limestone, Giralia Calcarenite and an unnamed siliceous limestone in the north of the island, formerly known as the 'Bossut Formation' (Hickman and Strong, 2003:61; Hocking et al., 1987). The most widespread unit, Trealla Limestone, is Middle Miocene in age while Giralia Calcarenite is Middle to Late Eocene. Boodie Cave is located within Trealla Limestone. Giralia Calcarenite is restricted to small outcrops in the centre of the island where some of the deeper valleys within Trealla Limestone occur. The siliceous limestone unit, however, is Quaternary in age and consists of lime-cemented shelly sand, dune sand and beach conglomerate. It is mostly restricted to the north of Barrow Island and occurs extensively through the Montebello Islands. Shellfish grazing on these limestone units may return radiocarbon ages much older than they should be – this is known as the hardwater effect.

Neritidae is a key family of molluscs dated in the Boodie Cave sequence. Nerites are herbivorous grazers found on rocky shorelines and mangroves on the littoral fringe. In

Hawaii, nerites feeding on Pleistocene limestone substrates can exhibit ΔR values of up to 990 ± 45 ^{14}C years (Dye, 1994). On Norfolk Island, nerites associated with calcareous sandstone substrates exhibited significant marine reservoir effects up to ΔR values of 1290 ^{14}C years (Anderson et al., 2001). To test the possible impact of these factors on dating nerites in the Boodie Cave sequence we subjected a single *Nerita albicilla* from the Australian Museum collection live-collected in the Montebello Islands in AD1912 to AMS analysis, yielding a ΔR value of 389 ± 20 ^{14}C years. This result indicates significant depletion of ^{14}C activity in this specimen, likely related to living on limestone substrates. However, a second herbivore collected in the Montebello Islands in the same year, *Turbo laminiferus*, yielded a ΔR of 130 ± 20 ^{14}C years (Table 1). This suggests the possibility of inter-specific and/or inter-habitat differences in ^{14}C pathways between contemporaneous specimens. Pending further investigation of marine reservoir effects for specific shellfish taxa living in the Barrow Island area, the calibrated ages on herbivorous shellfish should be treated as maxima.

The carnivore, *Melo* sp., was also subject to radiocarbon dating. Although there are no reservoir corrections published for *Melo* sp. on the CHRONO Marine Reservoir Correction database (Reimer and Reimer, 2001) (http://calib.qub.ac.uk/marine/), Ulm (2010) reports a single ΔR value on *M. amphora* collected in AD1907 from Mer in Torres Strait of 21 ± 30 ^{14}C years. This value is indistinguishable from the regional ΔR value recommended for eastern Torres Strait (Ulm, 2010). To specifically test ΔR in *Melo* sp., three specimens of *M. amphora* live-collected between AD1916 and AD1944 from Exmouth Gulf, Lacepede Islands and Sunday Island (King Sound) from the Australian Museum were AMS-dated to determine a pooled ΔR value of 62 ± 15 ^{14}C years (including external variance). This result

is in broad agreement with other ΔR values calculated for coastal areas dominated by the Leeuwin Current suggesting that the carnivorous feeding behaviours of *Melo* may not dramatically impact on their suitability for radiocarbon dating.

Tellina sp. was also dated. Several studies have suggested that *Tellina* sp. are potentially problematic for radiocarbon dating with anomalous values reported (Petchey, 2009). The anomalous values may be related to the feeding apparatus and habitat of *Tellina* sp. as they are a short-siphoned, sediment surface suspension feeder, with a preference for muddy substrates (Beesley et al., 1998:342-343). The potential magnitude of this problem is not known, however, dates on *Tellina* sp. from Mornington Island are in accord with dates on other shellfish species (Rosendahl, 2012).

A1.2 Single-grain optical dating

A1.2.1 Sample preparation and analysis

In total, 10 optically stimulated luminescence (OSL) samples were collected from Boodie Cave, seven of which were analysed at Adelaide University's Prescott Environmental Luminescence Laboratory (Ad14030 to Ad14036) and three of which were analysed at the Oxford University Luminescence Dating Laboratory (L008/15-1 to L008/15-3). OSL samples were collected from excavation squares A102/A103 and adjacent square A106 by inserting stainless steel tubes into freshly cleaned profiles. Bulk sediment samples were additionally collected from the OSL sample positions for dosimetry measurements and water content analyses.

Environmental dose rates were determined using high-resolution gamma spectrometry performed on dried and powdered bulk sediment for the Adelaide samples (Table A1), and

using inductively coupled plasma mass spectrometry (ICP-MS) for the Oxford samples (Tables A2). Isotopic concentrations and radionuclide activities were converted to external beta and gamma dose rates using published conversion factors (Guérin et al., 2011), beta attenuation factors (Adamiec and Aitken, 1998; Mejdahl, 1979), assuming radioactive equilibrium in the ^{238}U and ^{232}Th series. A relative uncertainty of 25% was applied to the measured water contents to account for possible variations in long-term hydrological conditions during burial. Cosmic ray contribution was calculated using the relationship between cosmic ray penetration, sample burial depth, bedrock overburden thickness, altitude, longitude and latitude (Prescott and Hutton, 1994). An internal dose rate of 0.03±0.01 Gy/ka was added to the total dose rate, based on published alpha efficiency factors, and ^{238}U and ^{232}Th values for etched quartz from a range of locations (Bowler et al., 2003).

The unexposed cores of the OSL sample tubes were prepared using standard procedures (Aitken, 1998), including etching by 48% hydrofluoric acid to remove the alpha irradiated external rinds of the purified quartz fractions. Etched grains were re-sieved to obtain the 180–250 μm fraction (Oxford) or 212–250 μm fraction (Adelaide), with the exception of Ad14033, for which the 125–180 μm fraction was used owing to limited quartz yields.

OSL measurements were carried out using a Risø TL/OSL-DA-20 (Adelaide) and TL/OSL-DA-15 (Oxford) reader equipped with a calibrated ^{90}Sr/^{90}Y β radiation source. Single-grain measurements were made by stimulating individual grains using a focused 10 mW green (532 nm) laser. Ultraviolet emissions were detected using an EMI 9235QB photomultiplier fitted with a 7.5 mm thick U340 filter. Single-grain OSL measurements were carried out by loading 180-250 and 212-250 μm quartz grains on 9.7 mm-diameter

discs each containing a 10 x 10 array of 300 μm diameter depressions (holes). For measurements made on the 125-180 μm fraction, single-grain discs with 200 μm depressions were used. Each single-grain disc position had previously been calibrated using precisely-dosed calibration quartz to account for spatial variations in the instrumental beta dose rate across the disc plane.

Equivalent dose (D_e) values were obtained for individual quartz grains using the single aliquot regenerative-dose (SAR) protocol (Murray and Wintle, 2000) (Table A3). Sensitivity-corrected dose-response curves were constructed using the first 0.17 s of each green laser stimulation after subtracting a mean background count obtained from the last 0.25 s of the signal. Between 200 and 800 quartz grains were measured per sample for D_e determination (Table 3). Individual grains were considered reliable for age calculation if they satisfied a series of standard and widely tested quality-assurance criteria, as detailed in Demuro et al. (2015).

Individual D_e estimates are presented with their 1 standard error ranges, which are derived from: (i) a random uncertainty term arising from photon counting statistics for each OSL measurement; (ii) an empirically determined instrument reproducibility uncertainty (1.9% or 2.5% for each single-grain OSL measurement performed on the Adelaide readers); and (iii) a dose-response curve fitting uncertainty determined using 1000 iterations of the Monte Carlo method described by Duller (2003) and implemented in Analyst.

The accepted grain D_e distributions and final OSL ages are summarised in Fig. A6 and Table 3. The final burial doses have been determined using either the central age model or 3-parameter minimum age model (Galbraith et al., 1999), depending on the type of D_e

scatter present, amount of observed overdispersion, and the outcomes of applying the log likelihood ratio test (Arnold et al., 2009).

A1.2.2 Analysis and interpretation of De distributions

The single-grain De distributions are presented as radial plots in Appendix Fig. A6D-M, and the final burial doses and ages are summarised in Table 3. The central age model, and 3- and 4-parameter minimum age models (CAM, MAM-3 and MAM-4) (Galbraith et al., 1999) have been applied on a sample-by-sample basis, depending on the type of De scatter present and the amount of observed overdispersion.

The overdispersion values for samples Ad14032, Ad14035 and Ad14036 range between 23% and 28% and are all within ±2σ of 20%, the global average for fully bleached and undisturbed samples (Arnold et al., 2011). These De datasets also appear consistent with a single dose population, and the majority of grains are well-represented by the weighted mean De value (as indicated by the large proportions of De values lying within the 2σ grey bands on the radial plots) (Appendix Fig. A6 F, I, J). These De characteristics suggest complete signal resetting before burial, and they do no not reveal any obvious signs of contamination by mixed grain populations. For these samples, the CAM is considered the most suitable age model, and has therefore been used to calculate the final ages (values shown in bold on Table A4).

Samples Ad14030, Ad14031, Ad14033, Ad14034, L008-15-1, L008-15-2 and L008-15-3 have higher overdispersion values of between 31% and 57%, which indicate more significant influences from extrinsic De scatter. Widespread post-deposition mixing is not thought to be a major contributor to single-grain dose dispersion at these sites given the

intact nature of the stratigraphy in the vicinity of the OSL samples (particularly the preservation of clear stratigraphic boundaries and absence of burrow features). Insufficient bleaching of grains prior to burial, or minor contamination by (unbleached) roof spall contaminants (quartz grains contained within the limestone bedrock), could account for older grain populations within these De datasets. We have therefore considered use of MAM-3 and MAM-4 in deriving burial dose estimates for these five samples. Beta dose rate heterogeneity (arising from microscale radionuclide variations in the surrounding sediments) could also account for both younger and older De populations in these single-grain datasets, and is therefore considered as a further cause of the observed higher overdispersion values.

The single-grain De distribution of sample Ad14030 exhibits a distinct 'leading edge' of low De values, an elongated tail of higher De values, and an asymmetric (positively skewed) spread of dose estimate, according to a previously developed test (Arnold and Roberts, 2009) (Appendix Fig. A6D). These characteristics are consistent with the poorly sorted nature of the host deposits and suggest that heterogeneous bleaching could account for the high overdispersion observed with this sample. This interpretation is further supported by statistical assessment of the CAM, MAM-3 and MAM-4 fits using a log likelihood ratio test (Arnold et al., 2009) (see Appendix Table A4 for further details of this approach). The MAM-3 LLIK score obtained for this dataset is more than 1.92 greater than the corresponding LLIK score for the CAM. This indicates that the inclusion of an extra model parameter improves the data fit, and the MAM-3 is better supported on statistical grounds. Application of the MAM-4 does not result in further significant improvement in the LLIK score when compared with the 95% C.I. of a X2 distribution (i.e. it does not

improve by at least 1.92), suggesting that the simpler MAM-3 explains the data just as well. Taking into consideration the log likelihood test results, De distribution characteristics and sedimentological properties of this sample, we have opted to use the MAM-3 for deriving a final burial dose estimate (Appendix Table A4).

Of the remaining six samples that display high overdispersion, three are characterised by broadly symmetric and unstructured De scatter (Ad14031, L008/15-3 and L008/15-2), and the other three contain sub-populations of relatively precise outlying De values on either or both sides of the weighted mean (Ad14033, Ad14034 and L008/15-1) (Appendix Fig. A6E, G, H, K, L, M). These De characteristics are not consistent with the aforementioned single-grain dataset of sample Ad14030, and they are not obviously indicative of heterogeneous bleaching prior to deposition. Application of the CAM is also statistically favoured over the MAM-3 and MAM-4 for these datasets according to the log likelihood ratio test (Arnold et al., 2009) (Appendix Table A4).

Some useful insights into the likely cause of the higher dose overdispersion for these six samples can be gleaned from the sedimentological properties of the host deposits. In particular, Ad14031, Ad14033, Ad14034 and L008/15-1 originate from sediments with potentially significant beta dose rate 'cold spots' or 'hot spots', which suggests that beta dose heterogeneity may partly or largely explain the presence of more scattered / outlying De values. Most notably, Ad14031 is derived from a unit with a distinct calcitic overgrowth, as well as abundant semi-angular pebbles. From a dose rate perspective, inert calcite precipitates are likely to represent radioactivity 'cold spots' in comparison to the surrounding silt- and clay-rich sediment matrix, whereas silicified pebbles may act as either beta dose rate hot spots or cold spots depending on their elemental composition. Ad14034,

Ad14033 and L008/15-1 were collected from layers with abundant pebbles. The former sample is additionally derived from a unit with relatively high feldspar and heavy mineral contents (potential beta dose rate hot spots), as well as abundant limestone roof fall material (potential beta dose rate cold spots). It therefore seems feasible that individual grains from sample Ad14031, Ad14033, Ad14034 and L008/15-1 experienced enhanced spatial variations in beta dose rates during their burial periods.

Intrinsic De scatter related to the experimental procedures could have further contributed to enhanced dose dispersion for these six samples; particularly as the most precise grains appear to yield high or low outlying De values for three of the samples (Ad14033, Ad14034 and L008/15-1) (Appendix Fig. A6G, H, M). These precise outliers may represent grains that are not responding favourably to the SAR measurement conditions (e.g. sub-populations of quartz grains with distinctly different geological origins, such as roof spall contaminants). Given the likely sources of De scatter affecting samples Ad14031, Ad14033, Ad14034, L008/15-1, L008/15-2 and L008/15-3 (namely beta dose heterogeneity and intrinsic dose dispersion), we have derived the final burial doses using the CAM (Table 3).

A1.3 Bayesian analysis

The Bayesian analysis used OxCal 4.2 (Bronk Ramsey, 2009a), with the aim of determining the most probable chronology by statistically treating the dates collectively. For these purposes a Sequence depositional model (Bronk Ramsey, 2008) is the most appropriate, with the only requirement of this model being that the dated determinations (or events) are entered into the model in the order of their deposition (Bronk Ramsey, 1998, 2008). An General t-type Outlier Model (Bronk Ramsey, 2009a) was also embedded into

the Sequence model where all dates were assigned a prior outlier probability of 0.05 (5%). The dated determinations are grouped in the model using four depositionally ordered Phases: SUs (stratigraphic units) 2, 3, 5 and 6–8. SUs 6–8 have similar (un-modelled) ages and so were grouped together (which also increases Phase sample size), while the ages contained within SUs 2, 3 and 5 illustrated enough intra-unit similarity and inter-unit differences to be modelled as separate groups. SU4 was not modelled because it does not occur in squares A102 and A103. Phases were separated by single uniform modelled boundaries (conforming to stratigraphic boundaries) following a contiguous model design (Bronk Ramsey 2009a). The one exception was the boundary between SUs 6 – 8 and SU5 which used two boundaries (following a sequential design; Bronk Ramsey 2009a) to mark the discontinuity between the strata. Boundaries provide probability density distributions (most probable date, and error range) for each stratigraphic boundary. The SU1 boundary was constrained in age, being allowed to occur only within a 500 year uniform distribution from 0 cal. BP. This prevents the model from predicting ages into the future. The ShCal (Hogg et al. 2013) and Marine13 (Reimer et al. 2013) curves were used for this model to calibrate dates on charcoal and shell respectively. Marine reservoir corrections (ΔR) for all dates on shell follow Sections 3.2.1 and A1.1.2.

Dates Wk-42541, OZU236, OZU237, OZU238 and OZU239 were manually rejected as outliers. Wk-42541 returned an uncalibrated age of 12250 ± 40 BP and occurs in a sterile unit, SU9, below a discontinuous stratigraphic boundary (above which are the oldest OSL determinations). The four OZU dates were obtained from small charcoal samples in the 4

mm and 2 mm wet sieve fractions and are likely contaminated. The 16 dates included in the Bayesian analysis are displayed in Fig. 4 and Tables A5–A6.

A1.4 Stratigraphy and sedimentological analyses

A1.4.1 Sediments and stratigraphic units

Boodie Cave contains nine stratigraphic units of which eight are present inside the cave in excavation squares A102/A103 (Fig. A7). The missing unit – Unit 4 – is a discrete marine-rich unit that has only been observed at the front of the cave (Veth et al., in press). The excavation reached ~ 180 cm depth, where sediments were culturally sterile, but did not reach bedrock. The cultural material in the upper SUs of Boodie Cave is diverse and extensive, with excavations uncovering very large assemblages of marine shell, terrestrial fauna, charcoal and stone artefacts.

The surface unit, Unit 1, is thin (< 10 cm) and comprises unconsolidated, poorly-sorted, fine to coarse-grained red-brown (5YR 4/4) sediments with abundant (20 - 30%) angular pebble-sized fragments of roof-fall material. The boundary between Unit 1 and Unit 2 is not sharp and is largely distinguished on the basis of the slightly lighter yellow-red colour (5YR 5/6) of Unit 2 and lower abundance of pebble-sized limestone fragments (~ 15%) but otherwise is similar to Unit 1. The transition to Unit 3 is again distinguished mainly by colour, although the boundary is partly obscured by gypsum overgrowth along most walls (Fig. A7). The average thickness of the unit is estimated at 15–20 cm. The sediments comprise darker red-brown (5YR 4/6), moderately sorted, coarse to fine sand with abundant (~ 25%) semi-rounded pebble-size limestone fragments with finely disseminated charcoal.

Unit 4 – a marine-rich unit – is not present inside the cave, hence the next unit transition is to Unit 5 and is more gradual. Unit 5 is the thickest (20–50 cm) unit and comprises a moderately compacted, moderately-sorted, dark red-brown (2.5YR 4/6) silty sand, again with abundant (~ 20%) pebbles and some larger charcoal fragments, evident of the more organic-rich nature of this unit. Unit 6 is similar to Unit 5 but lighter (2.5YR 4/8) with more pebble-sized limestone fragments (20–30%), and a concentration of cobble-size roof fall material on the north wall.

Unit 7 is a more compacted, well-sorted dark red (2.5YR 3/6) silty sand with increasing pebble and cobble sized roof-fall material (~ 25%), particularly on the south-east side of the square where a pebble lens essentially defines the boundary between Units 7 and 8 (Fig. A7). The transition to Unit 8 is marked both in terms of colour and texture (Fig. A7). Sediments in Unit 8 are finer grained and with fewer pebbles (~ 10–15%) except for a distinct pebble lens in the West wall (Fig. A7). Colour grades from a dark red (2.5YR 4/6) to a slightly lighter red (2.5YR 5/8) in the deeper part of the unit. The boundary between Unit 8 and the lowermost unit, Unit 9, is also marked both in terms of colour and texture (Fig. A7). The sediments comprise dark red brown (2.5YR 3/6), moderately to well-sorted clayey sand with very few pebbles (~ 5%), except for a discrete pebble lens is present at the base of the north wall.

A1.4.2 Micromorphology

Field records note roots and insect burrows throughout the profile, with some well disturbed areas mainly from single tree roots and fine rootlets. Micromorphological samples deliberately avoided these disturbed areas. Analyses were undertaken on 10 thin

(5 x 7.5 cm) sections made from orientated sediment casts from the North (A103) wall at depths of 130–150 cm, encompassing stratigraphic Units 7 to 9; and also from the South (A102) wall at depths of 0–35 cm and 70–95 cm, encompassing stratigraphic Units 1 to 3, Units 5 and 6 respectively (Fig. A7). Thin sections were prepared by Spectrum Petrographics, Washington, USA. Thin sections were observed using a Nikon polarizing petrographic microscope at the University of Western Australia, under plane polarized light (PPL) and crossed polarized light (XPL). An overview of micromorphological features for each stratigraphic unit is provided in Table A7 and Figures A8 and A9.

A1.4.3 Grain size analysis

Particle size analysis (< 2 mm fraction) was determined by Malvern Mastersizer 2000 (v. 5.6) at the University of Western Australia. Sediments were loose and only required minimal sonification (30 sec) and water as a dispersant (Fig. A10). Mastersizer analyses (Fig. A10) confirm a predominantly unimodal distribution in the uppermost part of the profile, changing to a bimodal distribution skewed towards the finer grain sizes in the middle units, and a distinct increase in finer modes in the basal units (Fig. A10). The main modal peak in the upper part of the profile is around 1100 μm. The middle units (SU3–SU6) are strongly bimodal with modal peaks between 480 – 640 μm and 75 μm (Fig. A10). There is a return to predominantly unimodal sediments in SU7 and SU8, albeit with slightly less coarse sand, with modal peak between 760–820 μm (Fig. SA10). The lowermost unit, SU9, shows a trimodal distribution with the main modal peaks at 69 μm, 4 μm and a smaller one at 370 μm (Fig. A10). This increase in fine sands towards the base of the profile may partly reflect the downward percolation of silts and clays (i.e. a pedogenic signature) but more likely reflects *in situ* disintegration of local bedrock within a largely closed cave

system. Microscopic examination of the sediments indicates that the very coarser (1000 μm) size fraction is predominantly comprised of carbonate, the coarse (500 – 1000 μm) and medium (200 – 500 μm) fraction comprises less carbonate and more silicates (with some bone), and the very fine fraction (< 100 μm) is predominantly comprised of silicates.

A1.5 Vertebrate taxa identification and analysis

The identification of vertebrate material is on-going and as such, will likely develop in terms of sample size and pattern complexity. Vertebrate fauna were identified with comparative skeletal reference material held at the Terrestrial Vertebrate Collections of the Western Australian Museum and the University of Queensland Archaeology Fauna Laboratory. Mammalian specimens were identified on the basis of teeth and associated cranial bones; reptile teeth and associated cranial bone, along with selected postcranial elements (vertebrae and in the case of marine turtle, all identifiable post-cranial bone) were identified; while in the case of fish, teeth were utilized for analysis, as cranial elements are absent. Skeletal specimens were identified to the lowest taxonomic level possible (Table A8, which also includes occurrence of *Scylla serrata*, mud crab).

A1.6 Aquatic invertebrate identification and analysis

Aquatic invertebrate finds include both marine and terrestrial shellfish as well as crustaceans and analyses are ongoing (examples presented in Fig. A12). All aquatic invertebrate remains from the 4 mm sieve fraction were sorted into the lowest taxonomic level. Minimum number of individuals (MNI), number of identified specimens (NISP) and shell weight per taxon were used to characterise shellfish abundance. tMNI was used which allowed for an increase in the MNI counts, especially for gastropods (Harris et al., 2015). Morphological attributes were measured for whole bivalve and gastropod shells following

Claassen (1998). All gastropod posterior and anterior fragments were measured as well as all bivalve hinges and umbos. All fragments of shell in their lowest taxonomic level were weighed and counted.

A1.7 Wood charcoal identification and analysis

Wood charcoal identification was undertaken following established procedures (Dotte-Sarout et al., 2015). Due to poor preservation, there were few charcoal fragments with anatomic integrity, preventing quantification. Analysis is based on the presence of identified taxa and their known preferred habitats, rather than their quantity. Each archaeological charcoal fragment was split by hand to reveal the three planes, and examined under a reflected light microscope. Anatomic features were compared to a regional wood anatomy database and charcoal reference collection. Wood is variable, even within individual species, consequently small differences in anatomic features were noted within the same taxon. Fragments with poor preservation and limited observable features were discarded from the analysis.

A1.8 Stable isotope analysis

Archaeological and modern tooth samples from *Lagorchestes conspicillatus* and *Macropus robustus* (Fig. A11) were collected from Barrow Island. Both species have limited home ranges, are mixed feeders and are non-obligate drinkers. Both species have limited home ranges, are mixed feeders and are non-obligate drinkers. Due the scarcity of archaeological teeth, the two species were grouped for analysis based on the strong similarities in their local distribution and feeding ecology (Brookman and Ambrose, 2012). Samples were prepared for analysis following established methods (Balasse, 2002; Garvie-Lok et al., 2004; Koch et al., 1997; Norman Wilson, 2013). Powdered tooth enamel samples from

premolars and molars formed post-weaning were treated overnight with 3% H_2O_2 to remove organic matter (40 µL of per 1.0 mg of enamel), followed by a 4-hr treatment with 0.1M acetic acid to remove diagenetic and absorbed carbonate. The carbonate phase of macropod tooth enamel is c. 5%. Approximately 6 mg samples of treated enamel (0.3 mg of carbonate) were analysed for $\delta^{13}C$ and $\delta^{18}O$ using an GasBench II coupled with Delta XL Mass Spectrometer (Thermo-Fisher Scientific) at the West Australian Biochemistry Centre, University of Western Australia (Paul and Skrzypek, 2007).

Appendix References

Adamiec, G., Aitken, M., 1998. Dose-rate conversion factors: update: Ancient TL 16, 37–50.

Aitken, M.J., 1998. An Introduction to Optical Dating: The Dating of Quaternary Sediments by the Use of Photon-stimulated Luminescence. Oxford University Press, Oxford.

Anderson, A., Higham, T., Wallace, R., 2001. The radiocarbon chronology on the Norfolk Island archaeological sites. Records of the Australian Museum, Supplement 27, 33–42.

Arnold, L. J., Roberts, R. G., 2009. Stochastic modelling of multi-grain equivalent dose (De) distributions: Implications for OSL dating of sediment mixtures. Quaternary Geochronology 4, 204-230.

Arnold, L.J., Roberts, R.G., Galbraith, R.F., DeLong, S.B., 2009. A revised burial dose estimation procedure for optical dating of young and modern-age sediments. Quaternary Geochronology 4, 306–325.

Arnold, L. J., Roberts, R. G., McPhee, R. D. E., Haile, J. S., Brock, F., Möller, P., Froese, D. G., Tikhonov, A. N., Chivas, A. R., Gilbert, T. P., Willerslev, E. 2011. Paper II – Dirt, dates and DNA: OSL and radiocarbon chronologies of perennially frozen sediments in Siberia, and their implications for sedimentary ancient DNA studies. Boreas 40. 417-445.

Balasse, M., 2002. Reconstructing dietary and environmental history from enamel isotopic analysis: time resolution of intra-tooth sequential sampling. International Journal of Osteoarchaeology 12, 155–165.

Beesley, P. L., Ross, G. J. B., Wells, A., 1998. Mollusca: the Southern synthesis. Fauna of Australia 5. CSIRO Publishing.

Bird, M.I., Levchenko, V., Ascough, P.L., Meredith, W., Wurser, C.M., Williams, A., Tilston, E.L., Snape, C.E., Apperley, D.C., 2014. The efficiency of charcoal decontamination for radiocarbon dating by three pre-treatments – ABOX, ABA and hypy. Quat. Geochronol. 22, 25–32.

Bowler, J. M., Johnston, H., Olley, J. M., Prescott, J. R., Roberts, R.G., Shawcross, W., Spooner, N.A., 2003. New ages for human occupation and climatic change at Lake Mungo, Australia. Nature 421, 837–840.

Bronk Ramsey, C., 1998. Probability and Dating. Radiocarbon 40, 461–474.

Bronk Ramsey, C., 2008. Radiocarbon Dating: Revolutions in Understanding. Archaeometry 50, 249–275.

Bronk Ramsey, C., 2009a. Bayesian Analysis of Radiocarbon Dates. Radiocarbon 51, 337–360.

Bronk Ramsey, C., 2009b. Dealing with Outliers and Offsets in Radiocarbon Dating. Radiocarbon 51, 1023–1045.

Brookman, T. H., Ambrose, S. H., 2012. Kangaroo tooth enamel oxygen and carbon isotope variation on a latitudinal transect in southern Australia: implications for palaeoenvironmental reconstruction. Oecologia 171, 403–416.

Claassen, C. Shells., 1998. In: Brothwell, D., Barker, G., Dincauze, D., Renouf, P. (Eds.) Cambridge manuals in archaeology. Cambridge University Press, Cambridge.

Culleton, B.J., Kennett, D.J., Ingram, B.L., Erlandson, J.M., Southon, J.R., 2006. Intrashell radiocarbon variability in marine mollusks. Radiocarbon 48, 387–400.

Demuro, M., Arnold, L. J., Parés, J. M., Sala, R., 2015. Extended-range luminescence chronologies suggest potentially complex bone accumulation histories at the Early-to-Middle Pleistocene palaeontological site of Huéscar-1 (Guadix-Baza basin, Spain). Quat. Int. 389, 191–212.

Dotte-Sarout, E., Xavier, C., Byrne, C., 2015. Not just carbon: assessment and prospects for the application of anthracology in Oceania. Archaeology in Oceania 50, 1–22.

Duller, G. A. T., 2003. Distinguishing quartz and feldspar in single grain luminescence measurements. Radiat. Meas. 37, 161–165.

Dye, T., 1994. Apparent Ages of Marine Shells: Implications for Archaeological Dating in Hawai'i. Radiocarbon 36, 51–57.

Fink, D., 2004. The ANTARES AMS facility at ANSTO. Nucl. Instrum. Methods Phys. Res. B 223-224, 109–115.

Franke, J., Paul, A., Schulz, M., 2008. Modeling variations of marine reservoir ages during the last 45 000 years. Clim. Past Discuss. 4, 81–110.

Friedman, G. M., 1959. Identification of Carbonate Minerals by Staining Methods. J. Sediment. Res. A Sediment. Petrol. Process. 29, 87–97.

Garvie-Lok, S. J., Varney, T. L. M., Anne, K., 2004. Preparation of bone carbonate for stable isotope analysis: the effects of treatment time and acid concentration. J. Archaeol. Sci. 31, 763–776.

Galbraith, R.F., Roberts, R.G., Laslett, G.M., Yoshida, H., Olley, J.M., 1999. Optical dating of single and multiple grains of quartz from Jinmium Rock Shelter, Northern Australia: Part 1, experimental design and statistical models. Archaeometry 41, 339–364.

Guérin, G., Mercier, N., Adamiec, G., 2011. Dose-rate conversion factors: update. Ancient TL 29, 5–8.

Harris, M., Weisler, M., Faulkner, P., 2015. A refined protocol for calculating MNI in archaeological molluscan shell assemblages: A Marshall Islands case study. J. Archaeol. Sci., 57, 168–179.

Hickman, A. H., Strong, C. A., 2003. Dampier Barrow Island: 1:250,000 Sheet, Western Australia. Geological Survey of Western Australia, Perth.

Hocking, R. M., Moors, H. T., Van de Graaff, J. E., 1987. Geology of the Carnarvon Basin, Western Australia. Geological Survey of Western Australia, Perth.

Hogg, A.G., Higham, T.F.G., Dahm, J., 1998. ^{14}C dating of modern marine and estuarine shellfish. Radiocarbon 40, 975–984.

Hogg, A. G., Hua, Q., Blackwell, P. G., Niu, M., Buck, C. E., Guilderson, T. P., Heaton, T. J., Palmer, J. G., Reimer, P. J., Reimer, R. W., Turney, C., Zimmerman, S. R. H., 2013. SHCal13 Southern Hemisphere Calibration, 0–50,000 Years cal BP. Radiocarbon 55: 1889–1903.

Hua, Q., Zoppi, U., Williams, A. A., Smith, A. M., 2004. Small-mass AMS radiocarbon analysis at ANTARES. Nucl. Instrum. Methods Phys. Res. B 223-224, 284–292.

Hua, Q., Jacobsen, G.E., Zoppi, U., Lawson, E.M., Williams, A.A., McGann, M.J., 2001. Progress in Radiocarbon Target Preparation at the Antares AMS Centre. Radiocarbon 43, 275–282.

Hua, Q., Webb, G.E., Zhao, J., Nothdurft, L.D., Lybolt, M., Price, G.J., Opdykee, B.D., 2015. Large variations in the Holocene marine radiocarbon reservoir effect reflect ocean circulation and climatic changes. Earth Planet. Sci. Lett. 422, 33–44.

Hogg, A.G., Hua, Q., Blackwell, P.G., Niu, M., Buck, C.E., Guilderson, T.P., Heaton, T.J., Palmer, J.G., Reimer, P.J., Reimer, R.W., Turney, C.S.M., and Zimmerman, S.R.H., 2013. SHCal13 Southern Hemisphere Calibration, 0–50,000 Years cal BP. Radiocarbon 55, 1889–1903.

Jacobs, Z., Duller, G. A. T., Wintle, A. G., 2006. Interpretation of single-grain De distributions and calculation of De. Radiat. Meas. 41, 264–277.

Komugabe-Dixson, A. F., Fallon, S. J., Eggins, S. M., Thresher, R. E., 2016. Radiocarbon evidence for mid-late Holocene changes in southwest Pacific Ocean circulation. Paleoceanography 31, 971–985.

Koch, P. L., Tuross, N., Fogel, M. L., 1997. The Effects of Sample Treatment and Diagenesis on the Isotopic Integrity of Carbonate in Biogenic Hydroxylapatite. J. Archaeol. Sci. 24, 417–429.

Mejdahl, V., 1979. Thermoluminescence dating: Beta-dose attenuation in quartz grains. Archaeometry 21, 61–72.

Mejdahl, V., 1987. Internal radioactivity in quartz and feldspar grains. Ancient TL 5, 10–17.

Murray, A. S., Wintle, A. G., 2000. Luminescence dating of quartz using an improved single-aliquot regenerative-dose protocol. Radiat. Meas. 32, 57–73.

Norman Wilson, J., 2013. Stable isotopes and trace elements in tooth enamel bioapatite: effects of diagenesis and pretreatment on primary palaeecological information. PhD thesis, Univ. South Florida.

O'Connor, S., Ulm, S., Fallon, S. J., Barham, A., Loch, I., 2010. Pre-Bomb Marine Reservoir Variability in the Kimberley Region, Western Australia. Radiocarbon 52, 1158–1165.

Paul, D., Skrzypek, G., 2007. Assessment of carbonate-phosphoric acid analytical technique performed using GasBench II in continuous flow isotope ratio mass spectrometry. Int. J. Mass Spectrom. 262, 180–186.

Petchey, F., 2009. New Directions in Archaeological Science Fairbairn, A., O'Connor, S., Marwick, B. (Eds.) ANU E Press, Canberra. pp.157–172.

Petchey, F., Anderson, A., Zondervan, A., Ulm, S., Hogg, A., 2008. New marine ΔR values for the South Pacific subtropical gyre region. Radiocarbon 50, 373–397.

Prescott, J.R., Hutton, J.T., 1994. Cosmic ray contributions to dose rates for luminescence and ESR dating: large depths and long-term time variations. Radiat. Meas. 23, 497–500.

Questiaux, D., 1991. Optical dating of loess: comparisons between different grain size fractions for infrared and green excited wavelengths. Nucl. Tracks Radiat. Meas. 18, 133–139.

Rees-Jones, J., 1995. Optical dating of young sediments using fine-grain quartz. Ancient TL 13, 9–14.

Reimer, P. J., Reimer, R. W., 2001. A Marine Reservoir Correction Database and On-Line Interface. Radiocarbon 43, 461–463.

Reimer, P.J., Baillie, M.G.L., Bard, E., Bayliss, A., Beck, J.W., Blackwell, P.G., Bronk Ramsey, C., Buck, C.E., Burr, G.S., Edwards, R.L., Friedrich, M., Grootes, P.M., Guilderson, T.P., Hajdas, I., Heaton, T.J., Hogg, A.G., Hughen, K.A., Kaiser, K.F., Kromer, B., McCormac, F.G., Manning, S.W., Reimer, R.W., Richards, D.A., Southon, J.R., Talamo, S., Turney, C.S.M., van der Plicht, J. and Weyhenmeyer, C.E., 2013. IntCal13 and Marine13 Radiocarbon Age Calibration Curves 0–50,000 Years cal BP. Radiocarbon 55, 1869–1887.

Rosendahl, D., 2012. The Way It Changes Like the Shoreline and the Sea: The Archaeology of the Sandalwood River, Mornington Island, Southeast Gulf of Carpentaria, Australia. PhD thesis, Univ. Queensland.

Southon, J., Santos, G., Druffel-Rodriguez, K., Druffel, E., Trumbore, S., Xu, X., Maya Mazo, M., Ali, S., Mazon, M., 2004. The Keck Carbon Cycle AMS Laboratory,

University of California, Irvine: Initial Operation and a Background Surprise. Radiocarbon 46, 41–49.

Squire, P., Joannes-Boyau, R., Scheffers, A. M., Nothdurft, L. D., Hua, Q., Collins, L. B., Scheffers, S. R., Zhao, J-X., 2013. A Marine Reservoir Correction for the Houtman-Abrolhos Archipelago, East Indian Ocean, Western Australia. Radiocarbon 55, 103–114.

Stuiver, M., Pearson, G.W., Braziunas, T., 1986 Radiocarbon age calibration of marine samples back to 9000 cal yr BP. Radiocarbon 28:980-1021.

Stoops, G., 2003. Guidelines for analysis and description of soil and regolith thin sections. Soil Science Society of America Inc.

Tanaka, N., Monaghan, M. C., Rye, D. M., 1986. Contribution of metabolic carbon to mollusc and barnacle shell carbonate. Nature 320, 520–523.

Ulm, S., 2002. Marine and estuarine reservoir effects in central Queensland, Australia: determination of ΔR values. Geoarchaeology 17, 319–348.

Ulm, S. 2010. Marine Carbon Reservoir Variability in Torres Strait Stage II: Progress Report for AINGRA08063. 2010. Available at: http://www.ainse.edu.au/__data/assets/pdf_file/0009/47349/r_08063.pdf (accessed 16.6. 2016).

Ulm, S., Petchey, F., Ross, A., 2009. Marine reservoir corrections for Moreton Bay, Australia. Archaeol in Oceania 43, 160-166.

UCI KCCAMS Facility, 2011a. Acid/Base/Acid (ABA) sample pre-treatment protocol - Internal Technical Report.

UCI KCCAMS Facility, 2011b. Leaching/hydrolysis protocol (carbonate samples) - Internal Technical Report.

Veth, P.M., Ward, I., Ditchfield, K., in press. Reconceptualising Last Glacial Maximum discontinuities: a case study from the maritime deserts of north-western Australia . J. Anthropol. Archaeol. http://dx.doi.org/10.1016/j.jaa.2016.07.016.

List of Tables

Agreement Index, 'OP' for outlier posterior and 'C' for convergence. Results for the first round of Bayesian analysis.

Table A7 Micromorphological description and post-depositional observations within sediments from Boodie Cave. Thin sections were observed using a Nikon polarizing petrographic microscope available at the School of Earth and Environment at UWA. Identification, description and semi-quantitative evaluation of particle abundance was done under plane polarized light (PPL) and crossed-polarized light (XPL) using different magnifications (2x, 5x, 10x, 25x) following existing terminology (Stoops, 2003).

Table A8 Identified faunal specimens grouped in stratigraphic units (SUs). Asterisk (*) designates fauna that were identified from squares at the front of the cave.

Table A9 $\delta^{18}O$ versus $\delta^{13}C$ for archaeological and modern macropod enamel (pM = permanent premolar, M3 = third molar, M4 = fourth molar). Isotopic results were standardised to the Vienna PeeDee Belemnite (VPDB) and given in per mil (‰). External error is < 0.10‰ for $\delta^{13}C$ and $\delta^{18}O$ (1st dev).

List of Figures

fragments in SU5, (f) carbonate precipitation around a bone fragment in SU6, (g) iron/manganese oxide hypocoating around bone fragment and sand grains in SU6.

Fig. A9 **Thin section microphotographs of resin impregnated sediments from stratigraphic units (SU) 7 to 9.** (a) Carbonate siltstone pebble in SU7, (b) lamellar calcrete and bone fragments at the top of SU7, (c) shell and bone material in SU8, (d) bone fragments and exotic tourmaline grains amongst dense granular (partially excremental) microstructure SU8, (e) plant fragment in SU8, (f) concentric (orthic) iron-nodule (possibly inherited) around limestone fragment at the base of in SU9, with dense excremental aggregates in surrounding groundmass, (g) sharp boundary (marked by arrow) between SU8 and SU9 marked by more dense granular microstructure. Plant fragments are also present in both units.

Fig. A10 **Summary of Mastersizer particle size analyses from various depths through the A103 sedimentary profile**. Results indicate a contrast from a predominantly unimodal distribution in the upper (youngest) units, bimodal sediments in the middle units, a return to unimodal sediments in the lower units and trimodal sediments in the lowermost (oldest) unit.

Fig. A11 **Example of teeth from excavation square A102/A103**. (a) Left lower third molar of *Lagorchestes conspicillatus* (A102, SU 4) and (b) Left lower first molar of *Macrotis lagotis* (A103, SU7). Scale bar is 10 mm.

Fig. A12 **Example of shell from excavation square A102/A103.** (a) Terebralia sp. fragments (A103, XU273), and sample (b) *Terebralia sp. operculum* (A103, XU278), (c) *Melo amphora* knife (E101, XU606), (d) Dentalium sp. bead (A103, XU242).

Appendix Tables

Table A1. High-resolution gamma spectrometry results and environmental dose rates for the Adelaide OSL samples collected from Boodie Cave.

Sample	Grain size (μm)	Sample depth (cm)	Water content (%) [a]	Radionuclide specific activities (Bq/kg) [b, c]						Environmental dose rate (Gy/ka) [d, e, f, g]				
				^{238}U	^{226}Ra	^{210}Pb	^{228}Ra	^{228}Th	^{40}K	Gamma dose rate	Beta dose rate	Cosmic dose rate	Internal dose rate	Total dose rate
Ad14030	212–250	5	3.5	7.8 ± 1.3	6.2 ± 0.5	5.6 ± 1.5	10.9 ± 1.1	11.0 ± 0.9	33 ± 2	0.20 ± 0.01	0.19 ± 0.01	0.08 ± 0.01	0.03 ± 0.01	0.49 ± 0.03
Ad14031	212–250	24	12.8	13.5 ± 2.4	11.2 ± 0.8	13.6 ± 3.0	17.9 ± 1.9	18.4 ± 1.6	108 ± 5	0.36 ± 0.03	0.42 ± 0.03	0.07 ± 0.01	0.03 ± 0.01	0.87 ± 0.06
Ad14032	212–250	68	10.4	19.7 ± 2.6	16.9 ± 1.5	18.2 ± 2.9	26.0 ± 2.4	26.7 ± 2.2	189 ± 7	0.55 ± 0.03	0.67 ± 0.04	0.07 ± 0.01	0.03 ± 0.01	1.32 ± 0.08
Ad14033	125-180	94	10.2	23.0 ± 3.0	20.8 ± 1.7	25.0 ± 3.7	33.9 ± 3.1	35.0 ± 2.9	237 ± 8	0.72 ± 0.04	0.88 ± 0.05	0.07 ± 0.01	0.03 ± 0.01	1.70 ± 0.10
Ad14034	212–250	142	18.4	27.4 ± 3.6	23.1 ± 1.6	29.9 ± 5.3	52.3 ± 4.7	53.6 ± 4.4	373 ± 13	0.97 ± 0.05	1.16 ± 0.06	0.06 ± 0.01	0.03 ± 0.01	2.22 ± 0.15
Ad14035	212–250	169	13.2	27.3 ± 3.6	22.2 ± 1.5	31.6 ± 4.8	53.7 ± 4.8	55.7 ± 4.5	416 ± 14	1.09 ± 0.06	1.31 ± 0.07	0.06 ± 0.01	0.03 ± 0.01	2.51 ± 0.15
Ad14036	212–250	193	7.3	17.4 ± 2.7	15.8 ± 1.1	17.0 ± 3.1	28.9 ± 2.7	32.2 ± 2.6	169 ± 7	0.59 ± 0.03	0.66 ± 0.04	0.06 ± 0.01	0.03 ± 0.01	1.34 ± 0.08

[a] Field water content is expressed as % of dry mass of mineral fraction and assigned relative uncertainties of ±25%.
[b] Measurements made on dried and powdered sediment sub-samples of ~120 g using high-resolution gamma-ray spectrometry (HRGS).
[c] Radionuclide specific activity uncertainties were derived from HRGS counting statistics, calibration standard uncertainties, and an empirically determined 2% fitting / reproducibility uncertainty for individual radionuclide activities.
[d] Dry dose rates were calculated from radionuclide activities using published conversion factors (Guérin et al., 2011).
[e] Cosmic-ray dose rates were calculated using a previous approach (Prescott and Hutton, 1994) and assigned a relative uncertainty of ±10%.
[f] The internal dose rate of 0.03 Gy/ka was assigned relative uncertainty of ±30%.
[g] Mean ± total uncertainty (68% confidence interval), calculated as the quadratic sum of the random and systematic uncertainties.

Table A2. Inductively coupled plasma mass spectrometry results and environmental dose rates for the Oxford OSL samples collected from Boodie Cave.

Sample	Grain size (μm)	Sample depth (cm)	Water content (%) [a]	Elemental concentrations [b]			Environmental dose rate (Gy/ka) [c, d, e, f]				
				U (ppm)	^{228}Th	K (%)	Gamma dose rate	Beta dose rate	Cosmic dose rate	Internal dose rate	Total dose rate
L008/15-3	180–250	47	12.5	1.4 ± 0.1	6.2 ± 0.6	0.9 ± 0.1	0.59 ± 0.04	0.83 ± 0.07	0.07 ± 0.01	0.03 ± 0.01	1.52 ± 0.11
L008/15-1	180–250	112	12.5	2.0 ± 0.2	11.3 ± 1.1	0.6 ± 0.1	0.80 ± 0.05	0.82 ± 0.06	0.06 ± 0.01	0.03 ± 0.01	1.71 ± 0.12
L008/15-2	180–250	138	12.5	2.2 ± 0.2	12.5 ± 1.2	0.6 ± 0.1	0.85 ± 0.06	0.87 ± 0.06	0.06 ± 0.01	0.03 ± 0.01	1.77 ± 0.13

[a] Field water content is expressed as % of dry mass of mineral fraction and assigned relative uncertainties of ±25%.
[b] Measurements made on dried and powdered sediment sub-samples of using inductively coupled plasma mass spectrometry.
[c] Dry dose rates were calculated from elemental concentrations using published conversion factors (Guérin et al., 2011).
[d] Cosmic-ray dose rates were calculated using a previous approach (Prescott and Hutton 1994) and assigned a relative uncertainty of ±10%.
[e] The internal dose rate of 0.03 Gy/ka was assigned relative uncertainty of ±30%.
[f] Mean ± total uncertainty (68% confidence interval), calculated as the quadratic sum of the random and systematic uncertainties.

Table A3 Single-aliquot regenerative-dose (SAR) procedure used in this study for (a) the Adelaide OSL samples, and (b) the Oxford samples. Each of these SAR measurement cycles was repeated for the natural dose, four different sized regenerative doses and a 0 Gy regenerative-dose to measure OSL signal recuperation. The smallest non-zero regenerative-dose cycle (and largest non-zero regenerative-dose cycle in the case of the Adelaide samples) was repeated at the end of the SAR procedure to assess the suitability of the test dose sensitivity correction. The smallest regenerative-dose cycle was also repeated a second time with the inclusion of step 2 to check for the presence of feldspar contaminants using an OSL-IR depletion ratio (Duller, 2003).

Step	(a) Adelaide Single-grain SAR protocol	(b) Oxford Single-grain SAR protocol	Signal / abbreviation
1	Dose (natural or laboratory)	Dose (natural or laboratory)	D_n or D_x
2 [a]	IRSL stimulation (50ºC for 60 s)	IRSL stimulation (50ºC for 60 s)	-
3	Preheat (260ºC for 10 s)	Preheat (260ºC for 10 s)	PH_1
4	Single-grain OSL stimulation (125ºC for 2 s)	Single-grain OSL stimulation (130ºC for 1 s)	L_n or L_x
5	Test dose (5 Gy)	Test dose (13 Gy)	D_t
6	Preheat (160ºC for 0 s)	Preheat (220ºC for 10 s)	PH_2
7	Single-grain OSL stimulation (125ºC for 2 s)	Single-grain OSL stimulation (130ºC for 1 s)	T_n or T_x
8	Repeat SAR measurement cycle for different D_x	Repeat SAR measurement cycle for different D_x	-

[a] Step 2 is only included in the single-grain SAR procedure when measuring the OSL-IR depletion ratio (Duller 2003). For Oxford, IRSL stimulation was at 20°C for 50 seconds (using 830 nm wavelength and 360 mW/cm^2 power).

Field and Laboratory Code	OD (%) [a]	CAM D_e (Gy) [b]	CAM LLIK score [c]	MAM-3 D_e (Gy) [b]	MAM-3 LLIK score [c]	MAM-4 D_e (Gy) [b]	MAM-4 LLIK score [c]	CAM age (ka) [b, d]	MAM-3 age (ka) [b, d]	MAM-4 age (ka) [b, d]
Ad14030	41±5	1.9 ± 0.1	-31.333	**1.5 ± 0.1**	-19.54	1.56 ± 0.1	-17.757	3.8 ± 0.4	**3.1 ± 0.3**	3.2 ± 0.3
Ad14031	47±4	**11.3 ± 0.6**	-72.895	6.3 ± 0.3	-84.49	5.5 ± 0.3	-72.828	**12.9 ± 1.2**	7.2 ± 0.7	6.3 ± 0.6
Ad14032	23±3	**23.9 ± 0.8**	-	-	-	-	-	**18.1 ± 1.2**	-	-
L008/15.3	46±4	**27.4 ± 1.4**	-84.414	20.5 ± 0.8	-107.645	18.7 ± 1.3	-104.559	**18.0 ± 1.6**	13.5 ± 1.2	12.3 ± 1.3
Ad14033	36±3	**72.5 ± 2.4**	-81.185	46.2 ± 2.5	-90.808	42.6 ± 2.8	-82.558	**42.5 ± 2.9**	27.1 ± 2.2	25.0 ± 2.2
L008/15.1	55±5	**87.4 ± 5.2**	-82.191	33.2 ± 2.8	-100.829	22.7 ± 4.5	-81.076	**51.1 ± 4.9**	19.4 ± 2.2	13.3 ± 2.8
Ad14034	31±4	**106.4 ± 5.3**	-26.897	79.4 ± 5.2	-29.483	74.1 ± 8.6	-25.391	**48.0 ± 4.1**	35.8 ± 3.4	33.4 ± 4.5
L008/15.2	57±5	**95.5 ± 5.7**	-81.284	34.6 ± 3.3	-103.809	31.1 ± 3.9	-86.987	**53.9 ± 5.3**	19.6 ± 2.4	17.6 ± 2.6
Ad14035	28±4	**123.4 ± 5.3**	-	-	-	-	-	**49.2 ± 3.8**	-	-
Ad14036	26±4	**103.6 ± 5.4**	-	-	-	-	-	**77.2 ± 6.1**	-	-

[a] The relative spread in the D_e dataset beyond that associated with the measurement uncertainties for individual D_e values, calculated using the CAM of Galbraith et al. (1999).
[b] Mean ± total uncertainty (68% confidence interval), calculated as the quadratic sum of the random and systematic uncertainties.
[c] LLIK represents the maximum log likelihood score of the CAM, MAM-3 or MAM-4 fit. For a given sample, the LLIK score of the MAM-3 is expected to be substantially higher (i.e. at least 1.92 greater) than that of the CAM when the addition of the extra model parameter improves the fit to the data. Likewise, the LLIK score of the MAM-4 is expected to be significantly greater than that of the MAM-3 (by at least 1.92 when compared with the 95% C.I. of a X^2 distribution) when the addition of the extra model parameter improves the fit to the data. If the extra parameter of the MAM-3 (or MAM-4) is not supported by the data, then its LLIK score will be similar to (i.e. within 1.92 of) the CAM (or MAM-3) LLIK score, indicating that the simpler age model explains the data just as well.
[d] Total uncertainty includes a systematic component of ±2% associated with laboratory beta-source calibration.

Table A4 Overdispersion (OD), central age model (CAM), 3-parameter and 4-parameter minimum age models (MAM-3 and MAM-4) D_e values and corresponding ages for the Boodie cave OSL samples. Ages shown in bold are considered most reliable according to the likelihood ratio test (LLIK score) outlined by Arnold et al. (2009). The MAM-3 and MAM-4 D_e estimates have been calculated after adding, in quadrature, a relative uncertainty of 15% to each individual D_e measurement error. This step was added to provide a minimum estimate of the underlying dose overdispersion observed in the single-grain dose-recovery test and in 'ideal' (well-bleached and unmixed) samples from these sites (sample AD14032), following previous models (Arnold and Roberts, 2009; Arnold et al., 2011). The MAM-3, MAM-4 and LLIK ratios were not applied to Ad14032, Ad14035 and Ad14036, as the overdispersion value of these three samples are all within ±2σ of 20%, the global average for fully bleached and undisturbed samples (Arnold and Roberts, 2009). These three D_e datasets are also well-supported by the CAM D_e value, as indicated by the large proportions of D_e values lying within the 2σ grey bands on the radial plots (Fig. A6 F, I, J).

Table A5 Results of Bayesian analysis. Two dates were found to be significant outliers: Wk-40403 (SU6) and Wk-40402 (SU5) were removed (see Table A6). The results returned Agreement Indices ($A_{overall}$ = 81.9%), outlier posterior probabilities and convergence values which suggest the model is robust and a better approximation of available age data. 'AI' stands for Agreement Index, 'OP' for outlier posterior and 'C' for convergence.

Name	Unmodelled (cal BP)							Modelled (cal. BP)							Indices		
	from (68.2%)	to (68.2%)	from (95.4%)	to (95.4%)	μ	σ	m	from (68.2%)	to (68.2%)	from (95.4%)	to (95.4%)	μ	σ	m	Agreement Index	Outlier Posterior	Convergence
Boundary: SU1 Top	1950	1450	1950	1450	1700	140	1700	1780	1450	1920	1450	1690	140	1690	100	-	100
Boundary: SU2/SU1	-	-	-	-	-	-	-	2940	1900	3390	1590	2500	520	2470	-	-	99.8
Phase: SU2																	
Ad-14030	3400	2800	3700	2500	3100	300	3100	3480	2870	3810	2540	3200	390	3180	98.9	94.7	99.5
Boundary: SU3/SU2	-	-	-	-	-	-	-	7040	6860	7110	6400	6850	350	6930	-	-	98.7
Phase: SU3																	
Wk-40396	7030	6910	7110	6870	6980	60	6970	7060	6950	7110	6900	7000	55	7000	97.5	97	99.8
Wk-40398	7110	6980	7150	6930	7040	60	7040	7090	6990	7140	6950	7040	50	7040	110.5	97.2	99.8
Wk-40399	7240	7020	7250	7010	7120	70	7110	7100	7010	7240	6990	7070	60	7060	101.7	96.7	99.7
Wk-40401	7040	6920	7120	6880	6990	60	6980	7060	6950	7120	6910	7010	50	7010	99.7	97.1	99.8
Boundary: SU5/SU3	-	-	-	-	-	-	-	7200	7020	7680	6970	7220	380	7130	-	-	98
Phase: SU5																	
Ad-14031	14100	11700	15300	10500	12900	1200	12900	14100	11600	15300	10500	12900	1240	12900	100	95.1	98.1
Wk-40400	12800	12700	12850	12700	12750	40	12750	12800	12700	18150	7050	12100	1950	12750	81.1	76.3	0.1
L008-15.3	19600	16400	21200	14800	18000	1600	18000	19200	16100	20650	14600	17650	1530	17650	102.3	95.2	97.8
Ad-14032	19300	16900	20500	15700	18100	1200	18100	19050	16700	20200	15500	17850	1200	17850	100.8	95.1	97.7
Boundary: SU5 Bottom								23850	17750	31500	16650	22400	4130	21250			96.6
Boundary: SU6 Top	-	-	-	-	-	-	-	34000	35700	40800	28400	36600	4400	37600	-	-	96.4
Phase: SU8 - SU6																	
Ad-14033	45400	39600	48300	36700	42500	2900	42500	44500	39600	47600	37700	42600	4950	42200	107.8	94.9	98.4
L008-15.1	56000	46200	60900	41300	51100	4900	51100	49200	40500	54600	38800	46200	5000	45700	75.9	94.8	96.9
Wk-42543	39800	38800	40400	38400	39400	500	39300	40000	38800	40800	38400	40400	9400	39500	94.5	93.8	98.7
Wk-42542	42100	41000	42500	40300	41500	550	41500	42100	40900	42600	40200	42300	9300	41500	98.9	94.4	99
L008-15.2	59200	48600	64500	43300	53900	5300	53900	50000	40500	55900	38900	46800	5350	46300	60.5	94.6	96.3
Boundary: SU8 Bottom	-	-	-	-	-	-	-	54700	41600	61400	41000	51100	10800	49600	-	-	55.2

Table A6 Results for the first round of Bayesian analysis. Two dates were found to be significant outliers: Wk-40403 (SU6) and Wk-40402 (SU5). These produce a significant impact on the model, not only in on the $A_{overall}$ statistic (72.4%) but also for boundary age estimation. These were removed and a second analysis run (see Table A5). 'AI' stands for Agreement Index, 'OP' for outlier posterior and 'C' for convergence. Results for the first round of Bayesian analysis.

Name	Unmodelled (cal BP)							Modelled (cal. BP)							Indices		
	from (68.2%)	to (68.2%)	from (95.4%)	to (95.4%)	μ	σ	m	from (68.2%)	to (68.2%)	from (95.4%)	to (95.4%)	μ	σ	m	Agreement Index	Outlier Posterior	Convergence
Boundary: SU1 Top	1950	1450	1950	1450	1700	140	1700	1770	1450	1920	1450	1690	140	1690	100		100
Boundary: SU2/SU1								2950	1890	3480	1550	2550	630	2490			99.8
Phase: SU2																	
Ad-14030	3400	2800	3700	2500	3100	300	3100	3490	2860	4010	2380	3270	570	3190	98.5	94.3	99.5
Boundary: SU3/SU2								7040	6860	7110	6390	6850	350	6930			99.2
Phase: SU3																	
Wk-40396	7030	6910	7110	6870	6980	60	6970	7050	6950	7110	6900	7000	50	7000	100	99.6	99.9
Wk-40398	7100	6980	7150	6930	7040	60	7040	7090	6990	7140	6950	7040	50	7040	113	99.6	99.9
Wk-40399	7240	7020	7250	7010	7120	70	7110	7100	7010	7240	6990	7070	60	7060	104.4	99.4	99.9
Wk-40401	7040	6920	7120	6880	6990	60	6980	7060	6950	7100	6910	7010	50	7010	102.2	99.6	99.9
Boundary: SU5/SU3								7200	7020	7690	6970	7220	385	7130			99
Phase: SU5																	
Ad-14031	14100	11700	15300	10500	12900	1200	12900	14150	11600	15450	10350	12900	1340	12900	100.5	95.5	96.6
Wk-40400	12800	12700	12850	12700	12750	40	12750	12800	12700	12850	12700	12750	40	12750	103.8	99.2	99.4
L008-15.3	19600	16400	21200	14800	18000	1600	18000	19550	16260	21150	14550	17850	1750	17850	101.3	95.2	96.4
Wk-40402	31300	31100	31500	30900	31200	140	31200	31600	12600	31600	7550	23000	7750	23000	43.5	38	0.1
Ad-14032	19300	16900	20500	15700	18100	1200	18100	19300	16780	20550	15450	18000	1420	18000	100.7	95.2	96.5
Boundary SU6/SU5								39200	18800	39900	17600	28000	7050	24800			7
Phase: SU8 - SU6																	
Wk-40403	25300	25000	25400	24600	25100	200	25100	41000	24500	45700	24500	31600	7700	25400	56.3	50.9	3.8
Ad-14033	45400	39600	48300	36700	42500	2900	42500	45000	39400	48000	37000	42300	2800	42300	103.3	95.4	95.8

L008-15.1	56000	46200	60900	41300	51100	4900	51100	51900	42400	56300	39100	47500	4500	47400	88.9	94.6	84.2
Wk-42543	39800	38800	40400	38400	39400	500	39300	39900	38800	40700	38300	39400	800	39400	99.7	95.5	97.6
Wk-42542	42100	41000	42500	40300	41500	550	41500	42100	40900	42600	40200	41500	650	41500	100.9	96.1	97.6
L008-15.2	59200	48600	64500	43300	53900	5300	53900	53300	42800	57800	39300	48400	4900	48300	76.8	94.1	80.8
Boundary: SU8 Bottom								58100	45010	65200	41800	53400	6900	52600			47.2

Table A7 Micromorphological description and post-depositional observations within sediments from Boodie Cave. Thin sections were observed using a Nikon polarizing petrographic microscope available at the School of Earth and Environment at UWA. Identification, description and semi-quantitative evaluation of particle abundance was done under plane polarized light (PPL) and crossed-polarized light (XPL) using different magnifications (2x, 5x, 10x, 25x) following existing terminology (Stoops, 2003).

	SU	Chronology (ky BP)	Slide no.	Micromorphological description	Microstructure/ groundmass	Pedofeatures
Holocene	**1**	2.5 – 1.7	**101**	Sub-angular limestone fragments (50%), burnt and unburnt bone (10%) and shell (5%) fragments, quartz (f.s. - m.s. 5 - 10%). Porosity ~ 5%.	Complex (intergrain) microstructure (c/f ratio 70:30), grading to compact (equal enaulic) microgranular fabric at unit boundary.	Disaggregated dung (plant and chiton) (5%). Very few impregnative Mn-oxide nodules and hypocoatings (mainly around limestone)
	2	6.8 – 2.5	**102, 103**	Sub-angular limstone fragments (25%). Decreased bone (inc. fewer burnt) fragments (5%), shell (2%), quartz (f.s. 5%)	Open enaulic microgranular structure (c/f ratio 40:60). Calcitic crystallitic b-fabric. Inter-aggregate porosity 20%.	Iron oxide impregnative coatings and hypocoatings around grains, and occasionally concentrated around voids
	3	7.2 – 6.8	**103**	Angular to sub-angular limestone (c.s. > 50%) with sub-rounded to well-rounded quartz (f.s. – c.s. 5%). Increased bone content (20%), minor shell (5-10%).	Moderately birefringent (limestone silt) groundmass, with speckled b-fabric (c/f ratio 80:20). Not compacted enaulic distribution. Inter-aggregate porosity 30%.	As above plus lenticular gypsum (m.s. – c.s.) infilling pore spaces (up to 20%), locally intergrown, forming massive aggregates, also in groundmass (5 - 10%).
Pleistocene	**5**	22.4 – 7.2	**104 - 106**	Angular to sub-angular limestone (c.s.) with sub-rounded to well-rounded quartz (f.s. – c.s. 10%), feldspars (< 5%). Bone (20 - 40%), plant fragments (8 – 10).	Compacted enaulic to porphyritic distribution (c/f ratio 30:70). Increased quartz (f.s. – m.s.) (20% groundmass). Calcitic crystallitic b-fabric. Inter-aggregate porosity < 20%.	Few infilled plant/insect burrows (1 – 2 mm diameter). Frequent impregnative Fe- and irregular Mn-oxide pedofeatures. Carbonate dissolution (pellicular weathering – Class I).
	6	42.6 – 36.6	**107**	Angular to sub-rounded limestone fragments (10%), feldspars (< 5%). Bone (15-20%), plant fragments (8 – 10).	Compacted enaulic to porphyritic distribution (c/f ratio 40:60), increased quartz (f.s. – m.s.) (< 40% groundmass). Inter-aggregate porosity 10%.	Frequent Fe-oxide impregnative coatings and hypocoatings around grains. Calcitic hypocoating around some bone fragments. Loose infilled oval plant/insect burrow (0.5 x 1 cm).
	7	46.2	**108**	Sub-rounded limestone fragments (10%), quartz (f.s. - c.s. 10%), feldspar (5%) and tourmaline grains (1%). Increased bone (20%), shell (2%), plant fragments (4 - 6).	Fine enaulic grading into porphytic (c:f ratio: 40: 60). Increased quartz (f.s. – m.s.) (< 50% groundmass). Calcitic crystallitic b-fabric. Inter-aggregate porosity < 20%.	Common impregnative Fe- and Mn-oxide pedofeatures of various morphologies. Common excremental aggregates.
	8	51.1 – 46.2	**109, 110**	Few large angular to sub-limstone fragments (20%), quartz (f.s. - m.s. 20%), feldspar (5%) and tourmaline (<1%). Bone (10-20%), eggshell (< 1%), plant fragments (2 - 4).	Open enaulic to granular microfabric (c/f ratio 80:20). Quartz (f.s. – m.s.) (~50% groundmass). Calcitic crystallitic b-fabric. Inter-aggregate porosity 40%.	Common impregnative Fe- and Mn-oxide pedofeatures. Frequent excremental aggregates. Single infilled longitudinal plant/insect burrow (width 3 mm).
	9	~ 77	**110**	Few large angular to sub-limstone fragments (10%), quartz (f.s. - m.s. 30%), feldspar (5%). Decreased bone (5-10%).	Compact (equal enaulic) microgranular structure. Quartz (f.s. – m.s.) (~50% groundmass). Calcitic crystallitic b-fabric. Inter-aggregate porosity 10%.	Few Fe- and Mn-oxide pedofeatures, with single concentric Fe-nodule around limestone. Carbonate dissolution (pellicular weathering – Class I)

Table A8 Identified faunal specimens grouped in stratigraphic units (SUs). Asterisk (*) designates fauna that were identified from squares at the front of the cave.

Observed Taxon	Common Name	SU 2	SU 3	SU 5	SU 6	SU 7	SU 8	Total
Mammal								
Dasyurus hallucatus	Northern quoll		2	5				**7**
Dasyurus geoffroii	Western quoll		5					**5**
Sarcophilus harrisi	Tasmanian devil			1				**1**
Perameles sp.	Long-nosed bandicoot		2					**2**
Perameles bougainville	Western barred bandicoot		6					**6**
Isoodon sp.	Short-nosed bandicoot		37	8				**45**
Isoodon auratus barrowensis	Golden bandicoot		24	2				**26**
Macrotis lagotis	Bilby		24	1		3		**28**
Trichosurus vulpecula	Brushtail possum		9					**9**
Bettongia lesueur	Burrowing bettong	3	48	12		1		**64**
Lagorchestes sp.	Hare-wallaby	1	6	1				**8**
Lagorchestes hirsutus	Rufous hare-wallaby	1	23	1	3			**28**
Lagorchestes conspicillatus	Spectacled hare-wallaby	5	45	7	8	3	2	**70**
Macropus sp.			5	2	3			**10**
Macropus robustus	Euro		9	3		5		**17**
Onychogalea unguifera	Northern nailtail wallaby	1						**1**
Petrogale sp.	Rock wallaby		13	4				**17**
Macropodidae	Macropod	1	22	12	1	3	2	**41**
Large Macropodidae	Large macropod		16	4	2	1	1	**24**
Medium Macropodidae	Medium macropod	3	50	3	1	2		**59**
Cetacea	Dolphin or small porpoise		*					
Reptile								
Cheloniidae	Hard-shelled sea turtle		10					**10**
Chelonia mydas	Green turtle		2					**2**
Scincidae	Skinks		22					**22**
Egernia sp.	Medium sized skink		10	1				**11**
Agamidae	Dragons		2					**2**
Varanus sp.	Monitors		5					**5**
Pythonidae	Pythons		18	3				**21**
Elapidae	Venomous snakes		4					**4**
Fish								
Balistidae	Trigger fish		1					**1**
Scaridae	Parrot fish		1					**1**
Labridae	Wrasse		7					**7**
Selachimorpha	Shark		*					
Crustaceans								
Scylla serrata	Mud crab		2					**2**
Total		**15**	**430**	**70**	**18**	**18**	**5**	**556**

Table A9 $\delta^{18}O$ versus $\delta^{13}C$ for archaeological and modern macropod enamel (pM = permanent premolar, M3 = third molar, M4 = fourth molar). Isotopic results were standardised to the Vienna PeeDee Belemnite (VPDB) and given in per mil (‰). External error is < 0.10‰ for $\delta^{13}C$ and $\delta^{18}O$ (σ).

Type	**Species**	**Molar**	**$\delta^{13}C$ (‰)**	**$\delta^{18}O$ (‰)**
Archaeological	*Lagorchestes conspicillatus*	M3	-7.29	1.03
Archaeological	*Lagorchestes conspicillatus*	M3	-5.29	4.41
Archaeological	*Macropus robustus*	pM	-3.84	0.65
Archaeological	*Macropus robustus*	M3	-1.88	0.44
Archaeological	*Lagorchestes conspicillatus*	M3	-4.99	3.57
Archaeological	*Lagorchestes conspicillatus*	pM	-4.64	2.38
Modern	*Lagorchestes conspicillatus*	pM	-6.49	-0.16
Modern	*Lagorchestes conspicillatus*	pM	-7.20	-1.43
Modern	*Lagorchestes conspicillatus*	M3	-9.61	-0.33
Modern	*Macropus robustus*	M3	-4.29	0.20
Modern	*Lagorchestes conspicillatus*	M3	-7.29	-1.01
Modern	*Lagorchestes conspicillatus*	pM	-6.90	-1.91
Modern	*Lagorchestes conspicillatus*	M3	-9.30	-0.98
Modern	*Lagorchestes conspicillatus*	M4	-5.75	-1.03
***t*-test (Archaeological/modern)**			**0.0264**	**0.0059**
Wilcoxon test (Archaeological/modern)			**0.0526**	**0.0007**

Appendix Figures

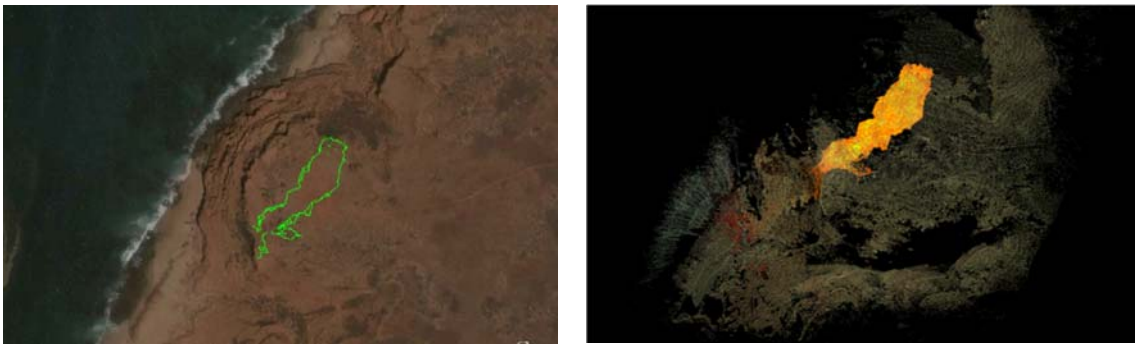

(a) (b)

Fig. A1 Cave outline overlaid with a satellite image taken from Google Earth (a), and the cave (orange) in the point cloud (b).

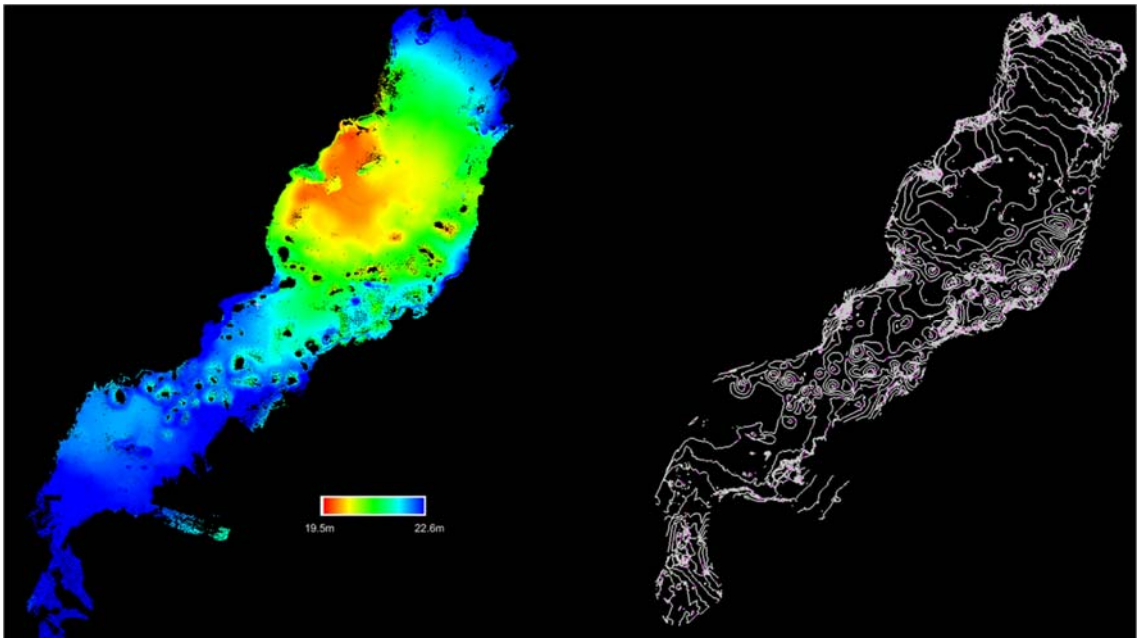

Fig. A2 Elevation and contour map of the cave floor.

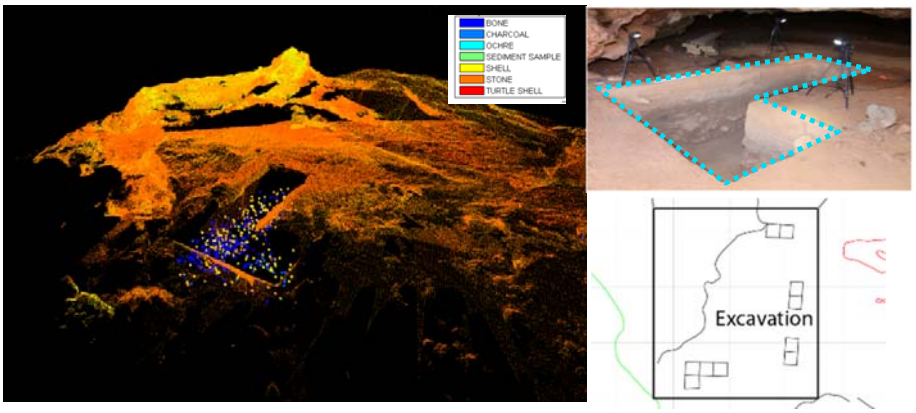

Fig. A3 Location of the artefacts within the excavation pit G101, F101, E101 in context of the surrounding area represented using the captured point cloud.

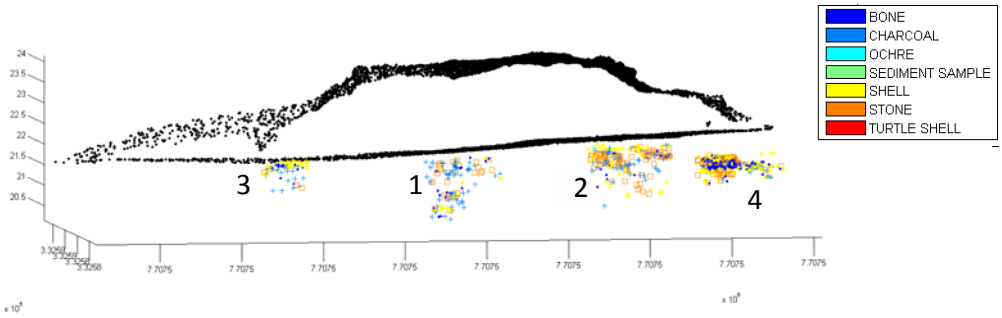

Fig. A4 Cross section of the cave with artefact locations.

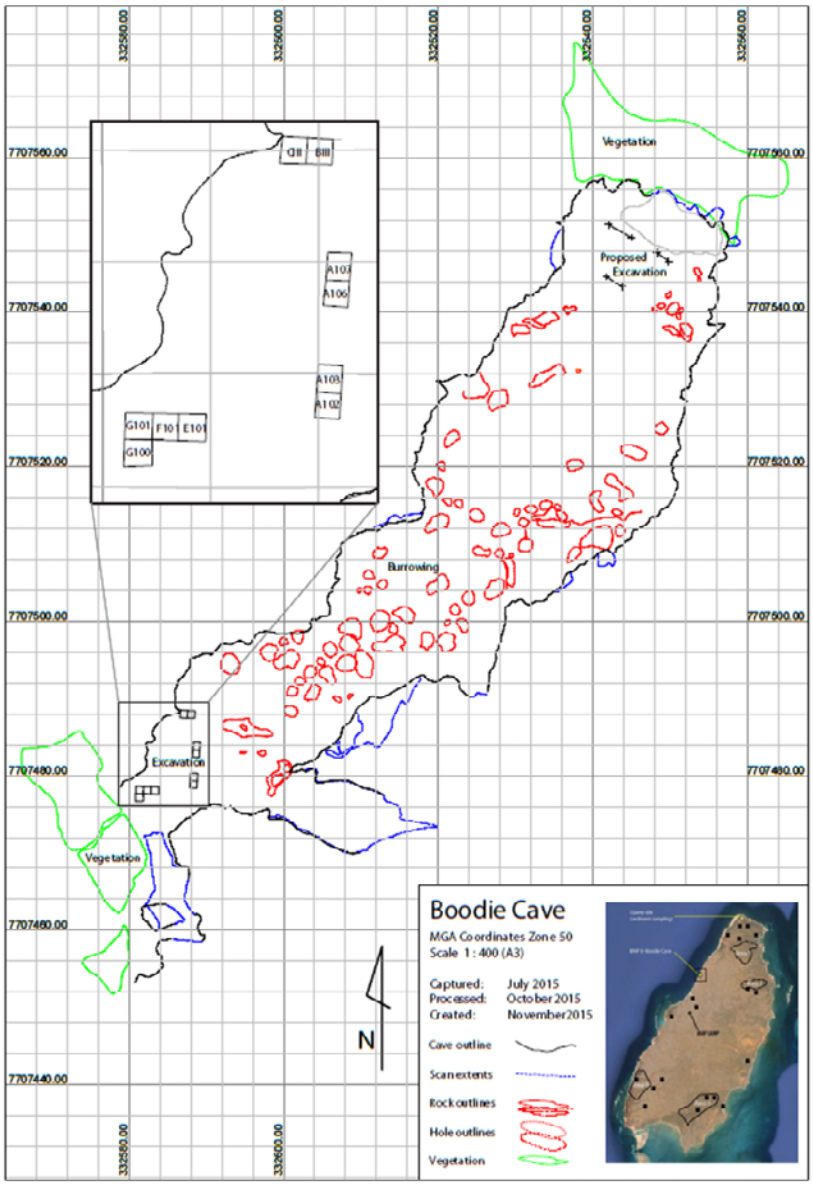

Fig. A5 **Plan of Boodie Cave rockshelter and excavation layout**. Traditional map information was extracted from the laser scanning point cloud and included site plans, locations of features, contour lines, profiles, as well as measurements and locations taken directly from the 3D point cloud. This paper is focused on adjacent 1 x 1 m excavation squares A102 and A103 (inset).

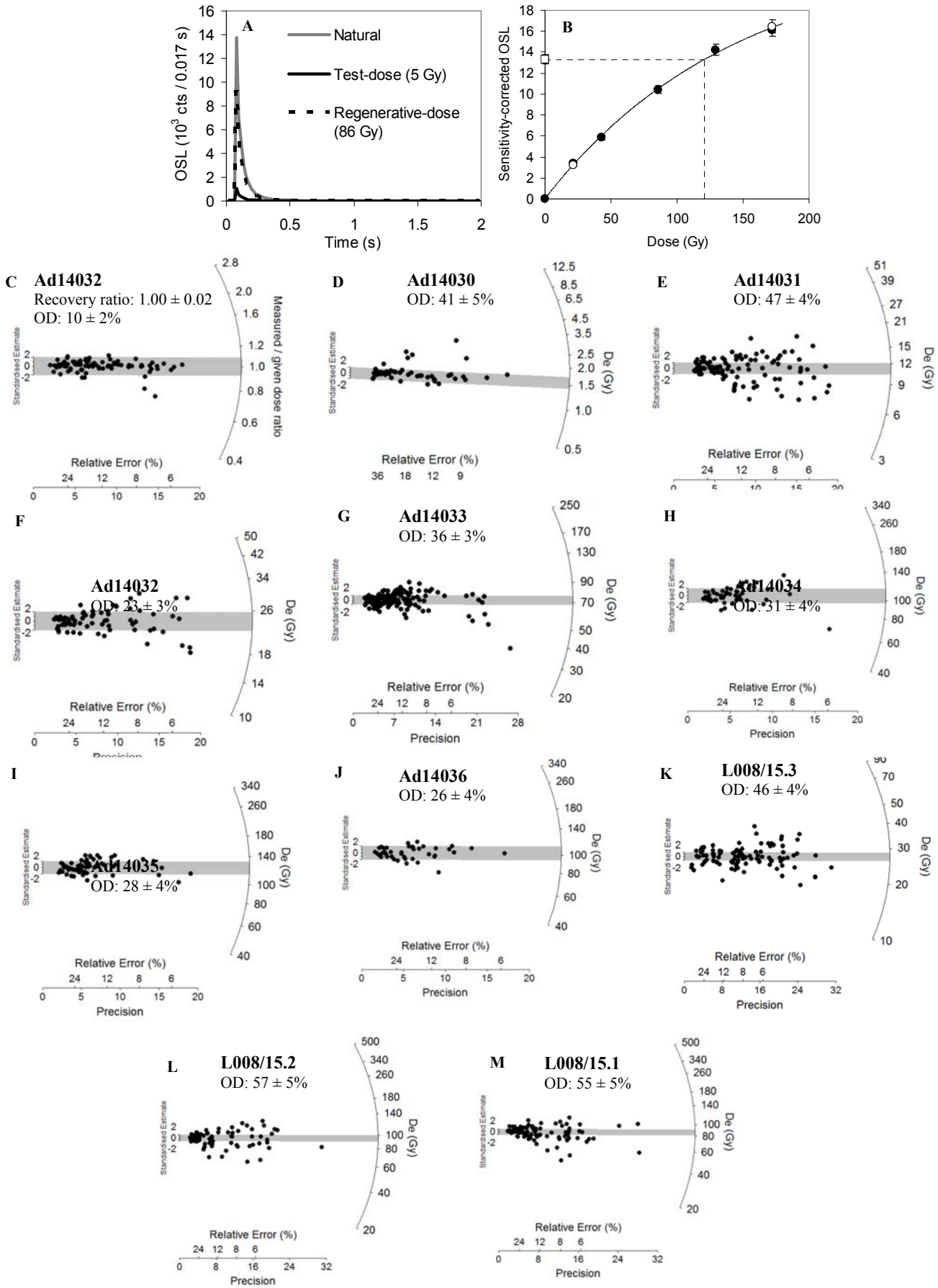
A
Natural
Test-dose (5 Gy)
Regenerative-dose (86 Gy)
OSL (10^3 cts / 0.017 s)
Time (s)
B
Sensitivity-corrected OSL
Dose (Gy)
C Ad14032
Recovery ratio: 1.00 ± 0.02
OD: 10 ± 2%
Measured / given dose ratio
D Ad14030
OD: 41 ± 5%
E Ad14031
OD: 47 ± 4%
F Ad14032
OD: 23 ± 3%
G Ad14033
OD: 36 ± 3%
H Ad14034
OD: 31 ± 4%
I Ad14035
OD: 28 ± 4%
J Ad14036
OD: 26 ± 4%
K L008/15.3
OD: 46 ± 4%
L L008/15.2
OD: 57 ± 5%
M L008/15.1
OD: 55 ± 5%
Standardised Estimate
De (Gy)
Relative Error (%)
Precision

Fig. A6 (a-b) OSL decay curves and sensitivity-corrected dose-response curve for a quartz grain of sample Ad14034 that passed the SAR rejection criteria. The dose-response curve was fitted using a single-saturating exponential function. (c) Single-grain OSL dose recovery test results for sample Ad14032 measured using the SAR protocol with a regenerative preheat of 260°C for 10 s and a test dose cut-heat of 160°C. The grey bar is centred on a measured to given dose ratio of 1 and the given dose was 25 Gy. (d-m) Radial plots showing the D_e distributions of the 10 samples from Barrow Island. The grey bar is centred on the CAM, with the exception of sample Ad14030, which is centred on the MAM-3.

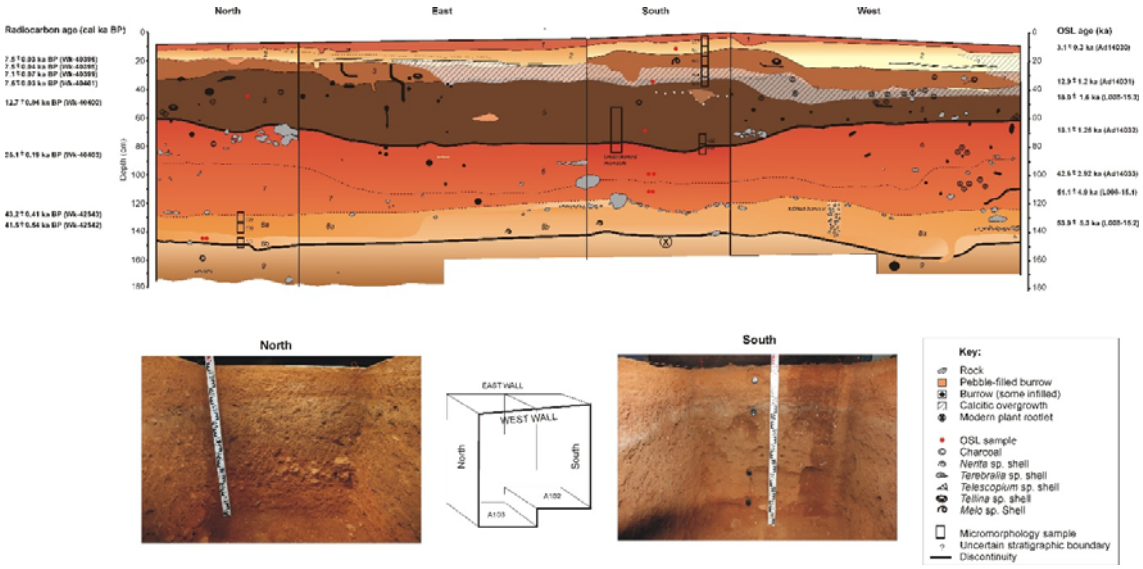

Fig. A7 **Section drawing of Boodie Cave square A102/A103 and upper profile of North and South walls**. Pebble-size limestone fragments are present throughout the profile, and are concentrated at a boundary between stratigraphic units 7 and 8 on the South wall. Cobble-size material is concentrated in stratigraphic units 3 and 6, particularly on the North wall. White gypsum overgrowth is evident across the East, South and West walls around the level of stratigraphic unit 3. Insect burrows and plant roots are mainly concentrated on the West wall and the upper part of the East wall and are most likely associated with more recent growth of *Ficus* sp. plants at the front of the cave. An infilled burrow in stratigraphic unit 8 on the West wall appears to be truncated by the overlying unit, hence is syn-depositional in origin. Dates are as provided from radiocarbon (table 2) and luminescence (table 3, A1-4) analyses.

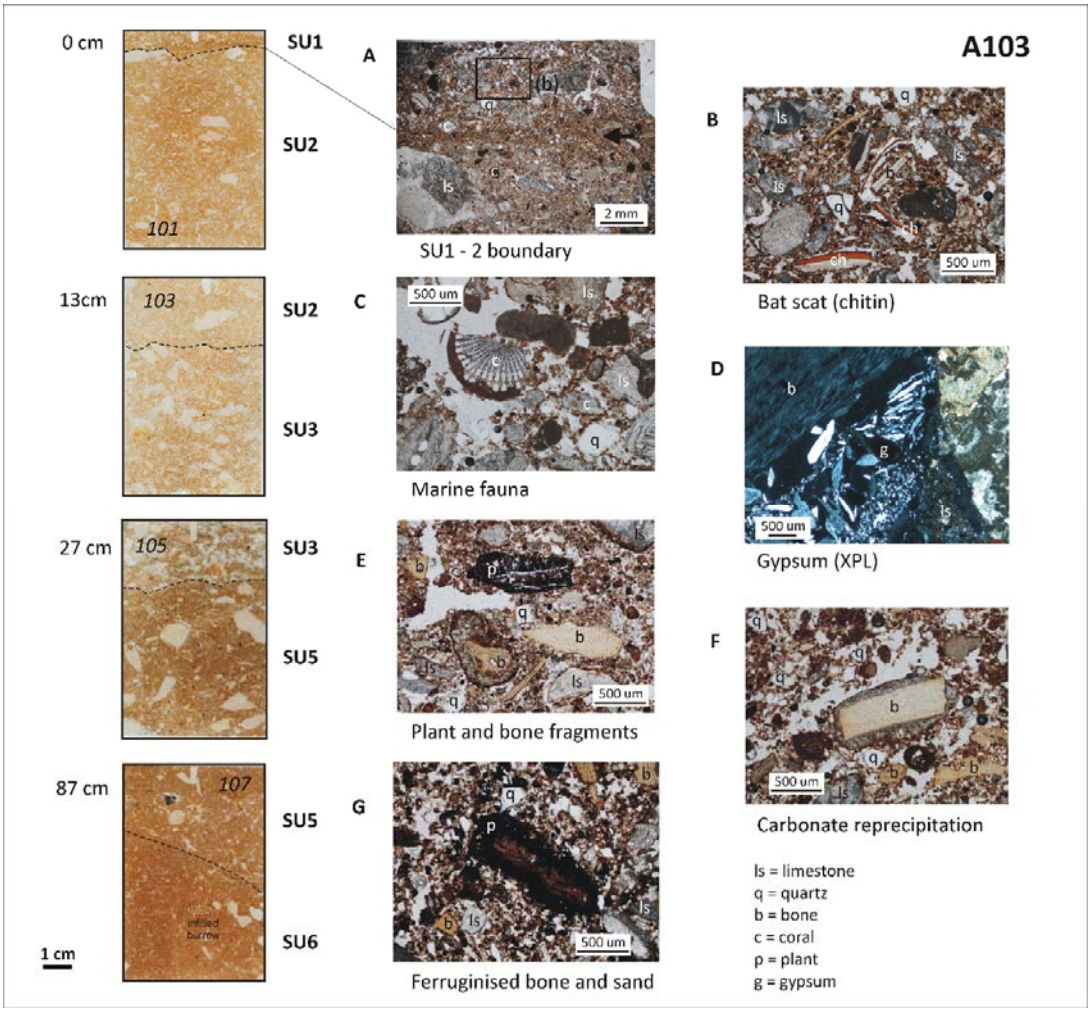

Fig. A8 **Thin section microphotographs of resin impregnated sediments from stratigraphic units (SU) 1 to 6.** (a) Compacted ferruginous sediments marking the boundary between the loose surface sediments (SU1) and SU2, (b) inset from image (a) showing chitin fragments from bat scats within poorly sorted sands, (c) ferruginised coral fragment in SU2, (d) gypsum formation within interspace between bone and limestone fragments, (e) plant and bone fragments in SU5, (f) carbonate precipitation around a bone fragment in SU6, (g) iron/manganese oxide hypocoating around bone fragment and sand grains in SU6.

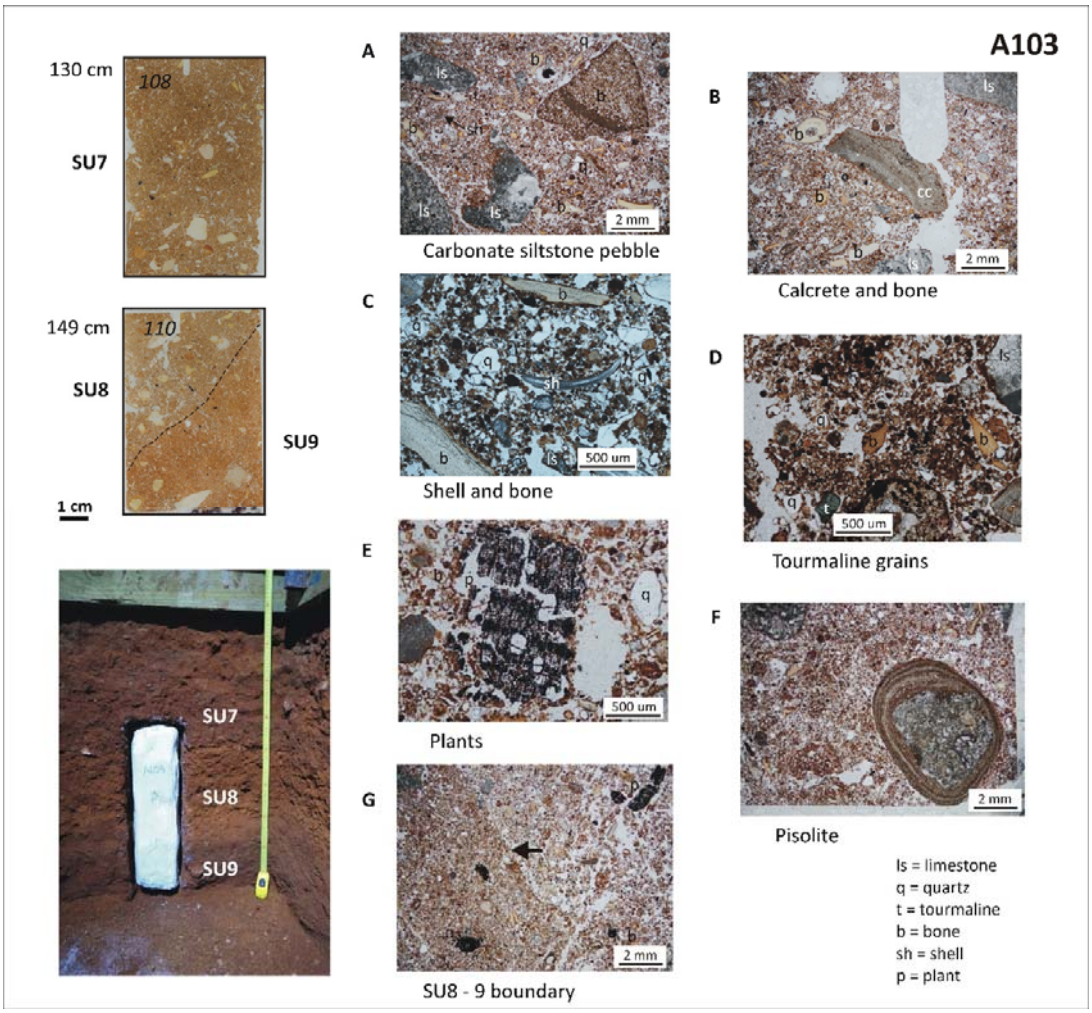

Fig. A9 **Thin section microphotographs of resin impregnated sediments from stratigraphic units (SU) 7 to 9.** (a) Carbonate siltstone pebble in SU7, (b) lamellar calcrete and bone fragments at the top of SU7, (c) shell and bone material in SU8, (d) bone fragments and exotic tourmaline grains amongst dense granular (partially excremental) microstructure SU8, (e) plant fragment in SU8, (f) concentric (orthic) iron-nodule (possibly inherited) around limestone fragment at the base of in SU9, with dense excremental aggregates in surrounding groundmass, (g) sharp boundary (marked by arrow) between SU8 and SU9 marked by more dense granular microstructure. Plant fragments are also present in both units.

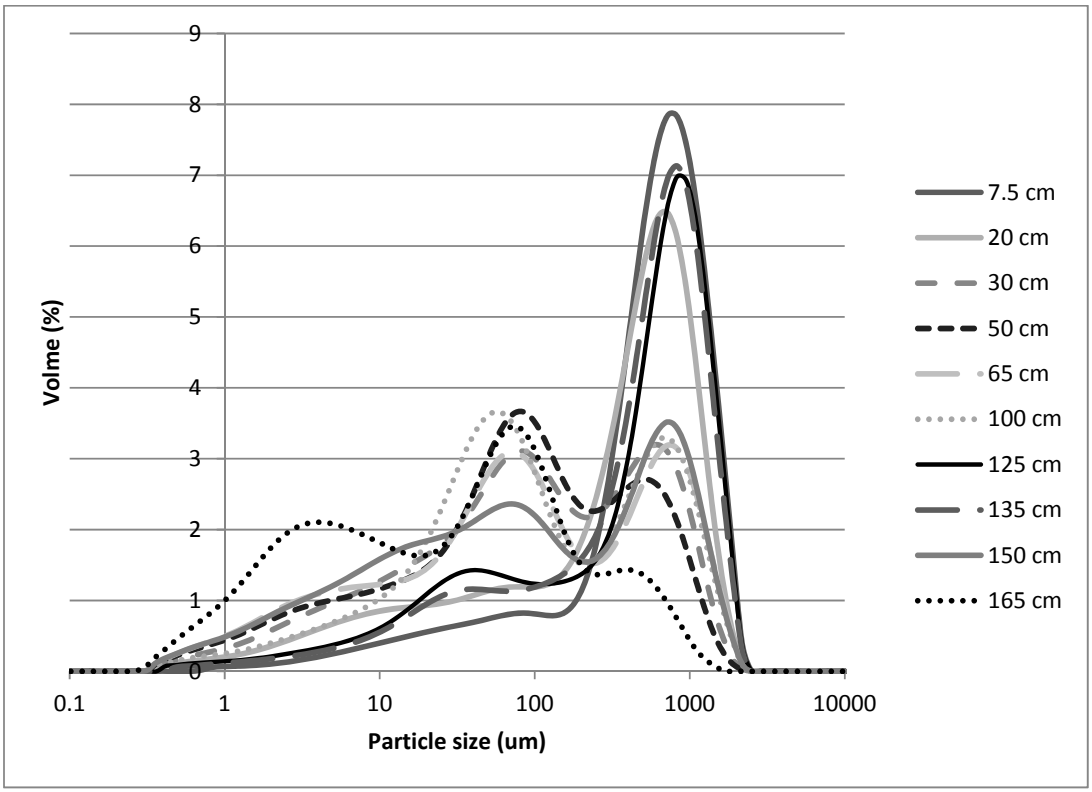

Fig. A10 Summary of Mastersizer particle size analyses from various depths through the A103 sedimentary profile. Results indicate a contrast from a predominantly unimodal distribution in the upper (youngest) units, bimodal sediments in the middle units, a return to unimodal sediments in the lower units and trimodal sediments in the lowermost (oldest) unit.

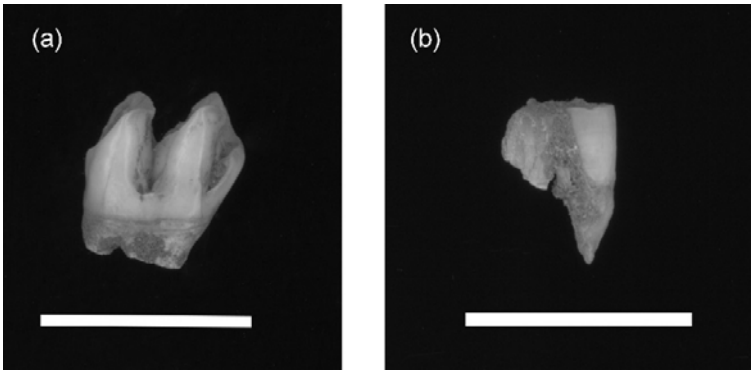

Fig. A11 Example of teeth from excavation square A102/A103. (a) Left lower third molar of *Lagorchestes conspicillatus* (A102, SU 4) and (b) Left lower first molar of *Macrotis lagotis* (A103, SU7). Scale bar is 10 mm.

Fig. A12 Example of shell from excavation square A102/A103. (a) *Terebralia* sp. fragments (A103, XU273), and sample (b) *Terebralia* sp. *operculum* (A103, XU278), (c) *Melo* sp. dentate knife (E101, XU606), (d) *Dentalium* sp. bead (A103, XU242).

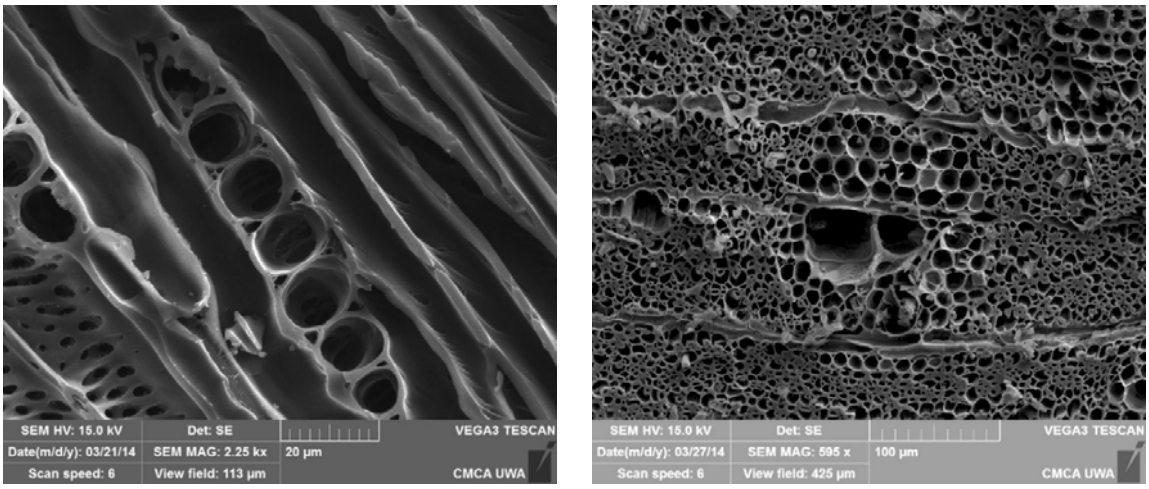

Fig. A13 Example of plant charcoal. Left = *Acacia coriacea* ray. Right = *Acacia pyrifolia* vessels with confluent parenchyma cells.

Fig. A14 **Example of macropod teeth used for isotopic analysis from excavation square A103.** Sample (a) Right maxilla fragment of *Macropus robustus* (from XU260), and sample (b) Left mandible fragment of *Lagorchestes conspicillatus* (from XU255).

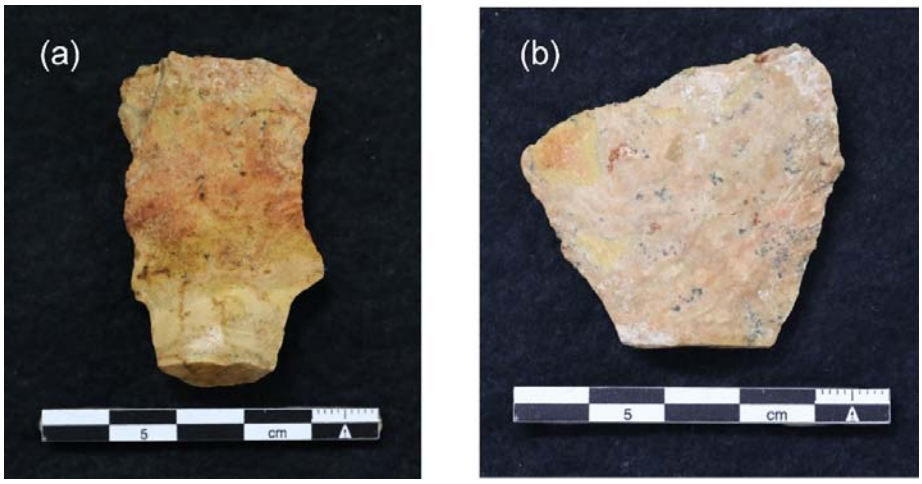

Fig. A15 Example of limestone lithics from Boodie Cave. (a) Ventral surface of a limestone flake (A106, XU31), and (b) Ventral surface of a limestone flake (A102, XU221).